The η Aquilae System: Radial Velocities and Astrometry in Search of η Aql B

G. Fritz Benedict[1] , Thomas G. Barnes, III[1] , Nancy R. Evans[2] , William D. Cochran[1] , Richard I. Anderson[3] ,
Barbara E. McArthur[1], and Thomas E. Harrison[4]

[1] McDonald Observatory, University of Texas, Austin, TX 78712, USA
[2] Harvard-Smithsonian Center for Astrophysics, Cambridge, MA 02138, USA
[3] Institute of Physics, Laboratory of Astrophysics, École Polytechnique Fédérale de Lausanne (EPFL), Observatoire de Sauverny, 1290 Versoix, Switzerland
[4] Department of Astronomy, New Mexico State University, Box 30001, MSC 4500, Las Cruces, NM 88003-8001, USA
Received 2021 August 9; revised 2022 April 19; accepted 2022 April 19; published 2022 May 20

Abstract

The classical Cepheid η Aql was not included in past Leavitt Law work because of a presumed complicating orbit due to a known B9.8V companion. To determine the orbit of η Aql B, we analyze a significant number of radial velocity (RV) measurements from eight sources. With these we establish the RV variation due to Cepheid pulsation, using a model with 12 Fourier coefficients, while solving for velocity offsets required to bring the RV data sets into coincidence. RV residuals provide no evidence of orbital motion, suggesting either nearly face-on orientation or a very long period. Reanalysis of Hubble Space Telescope Fine Guidance Sensor astrometry now includes reference star parallax and proper motion priors from Gaia EDR3. As modeling confirmation, we reanalyze ζ Gem in parallel, deriving values for its parallax and proper motion consistent with Gaia EDR3, and consistent with the Benedict 2007 Leavitt Law. In an effort to further characterize η Aql B, we hypothesize that η Aql residuals larger than those of the associated reference stars or a parallax inconsistent with EDR3 and the Benedict 2007 Leavitt Law indicate unmodeled orbital motion. Using the astrometric noise or parallax mismatch with EDR3, we estimate possible periods and mass for η Aql B. Ascribing photocenter motion to the photometric variation of the Cepheid, η Aql A, yields a plausible separation that is consistent with a long period and explains the lack of RV variation. None of these approaches yields an unassailable characterization of the η Aql A–B system.

Unified Astronomy Thesaurus concepts: Young disk Cepheid variable stars (1832); Cepheid variable stars (218)

Supporting material: machine-readable tables

1. Introduction

Cepheids are prime objects for distance determination using a period–luminosity relation, now known as the Leavitt Law (hereafter, LL). To confirm our understanding of pulsation, identifying Cepheids in binary or multiple systems from which masses can be measured also has high value.

η Aql was in fact the first Cepheid in which light variation was discovered, by Pigott in 1784, having preceded the discovery of variation in δ Cep itself by only weeks. It has comparatively well-behaved variation with a period of 7.18 days.

An early observation with the International Ultraviolet Explorer (IUE) satellite found not the low flux of a cool Cepheid, but a strong ultraviolet flux from a hot star (Mariska et al. 1980), which was surprising since a series of radial velocity studies in the 20th century showed no clear indication of orbital motion. UV spectrophotometry of η Aql B (Table 8, Evans 1991) further confirmed the connection of η Aql B with η Aql A. That result, if components A and B have the same distance from us, indicated an absolute magnitude range for η Aql A of $-3.39 > M_V > -3.74$ (depending on IUE spectrum wavelength and/or which model atmosphere was used), which with $V - K = 1.89$ yields $-5.28 > M_K > -5.63$, agreeing with the Benedict et al. (2007) LL within the Evans (1991) range.

This further supports the assertion that components A and B are *not* a chance alignment.

η Aql was observed by the Hubble Space Telescope (HST) Fine Guidance Sensor (FGS) in a program to determine Cepheid parallaxes (Benedict et al. 2007). Unfortunately, it was the one star in that program for which a parallax could not be determined because of perturbations thought to be from binary motion. But, with no information about an orbit with which to model them, η Aql remained without an FGS parallax.

Using the Wide Field Camera 3 (WFC3) on HST, Evans et al. (2013) found a companion $0\rlap{.}{''}66$ from the Cepheid. Subsequently, Gallenne et al. (2014) found the same companion with the NACO instrument on the ESO Very Large Telescope. They estimated the unreddened H magnitude to be 9.34 ± 0.04, corresponding to the spectral type range F1V to F6V.

These results combine to present the following picture of the η Aql system. In addition to the Cepheid, it contains a resolved companion with an F spectral type (component C) and a hot third star (component B) closer to the Cepheid with a spectral type of B9.8V (Evans 1991).

We note that there has recently been interest in the occurrence of triple systems as well as binaries. The distributions of parameters of binaries and higher multiples (mass ratio, separation, eccentricity) are important constraints in modeling star formation. In addition, the interaction between components of a triple system via the Kozai–Lidov mechanism (e.g., Naoz 2016) plays an important role in post-formation evolution of the system.
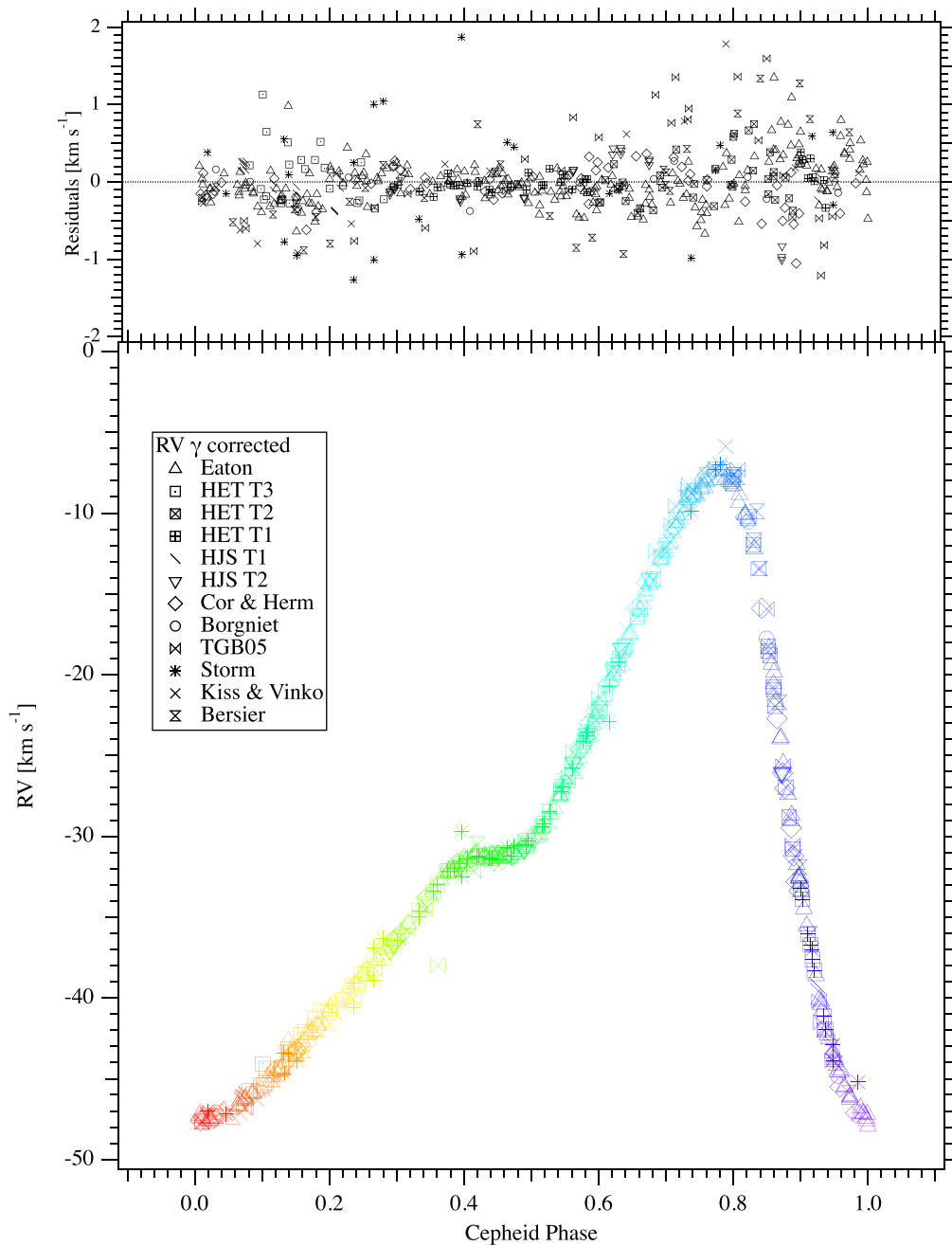
Figure 1. The γ-corrected RV (γ corrections produced by the Fourier modeling of pulsational RV, coefficients listed in Table 6), plotted as a function of quadratic phase (Equation (1)). We list the RV sources and associated γ values in Table 5. We color-coded the RV values by Cepheid phase (red = 0 to blue = 1). Residuals are in the upper panel.

We revisit η Aql, now with new high-precision radial velocities (RVs) from the Hobby–Eberly Telescope (HET), the Harlan J Smith telescope of McDonald Observatory, the Hermes Spectrograph on the Mercator Telescope, and the Coralie spectrograph on the Euler telescope. Our goals included measuring a parallax for η Aql, establishing a perturbation orbit for η Aql A (assisted by orbit information derived from RV), and obtaining a dynamical mass for the hot companion, η Aql B. We first present how we obtained (Section 2.2) and reduced (Section 2.3) our new, high-precision RV data. We next derive a Fourier description of the RV pulsation signal, and fail to identify the signature of an η Aql B perturbation orbit in the residuals to that pulsation model (Section 2.5). Section 3 presents our analysis of the

HST astrometry, yielding a parallax for η Aql and weak evidence for an astrometric perturbation. We place η Aql on the Benedict et al. (2007) LL, estimate an orbital period range for the B9.8V companion, discuss remaining issues in Section 4, and summarize in Section 5.

For the astrometry we abbreviate milliarcsecond to mas, and transform Julian Day to a truncated Julian Date, TJD = JD – 2,400,000.

2. Radial Velocities

2.1. Pulsational Phase

η Aql has an evolving pulsational period (Berdnikov et al. 2000; updated based on Engle 2015), which complicates

Table 1
HET Radial Velocities

Template	TJD[a]	Phase	RV[b]	Error
1	55,421.6832	0.392987	14.291	0.037
1	55,432.6456	0.920442	7.699	0.042
1	55,432.7468	0.934547	4.856	0.051
1	55,450.6017	0.422376	14.790	0.039
1	55,451.5960	0.560923	20.209	0.043
1	55,458.6719	0.546853	19.075	0.042
…	…	…	…	…

Notes.
[a] Julian Day − 2,400,000.
[b] Relative velocity in km s^{-1}. See Table 5 for correction to absolute velocity.

(This table is available in its entirety in machine-readable form.)

Table 2
HJS Radial Velocities

Template	TJD[a]	Phase	RV[b]	Error
1	58,376.5856	0.116495	−7.841	0.184
1	58,376.5873	0.116735	−7.945	0.171
1	58,376.5891	0.116979	−7.735	0.199
1	58,390.6463	0.075647	−9.126	0.170
1	58,390.6476	0.075830	−9.045	0.172
1	58,390.6489	0.076014	−8.996	0.178
…	…	…	…	…

Notes.
[a] Julian Day − 2,400,000.0
[b] Relative velocity in km s^{-1}. See Table 5 for correction to absolute velocity.

(This table is available in its entirety in machine-readable form.)

computation of the pulsation phase. Phase can be calculated from

$$\mathrm{HJD_{pred}} = 2{,}411{,}999.693 + 7.17654682E \\ + (2.90 \times 10^{-8})E^2 \qquad (1)$$

where $\mathrm{HJD_{pred}}$ is the Heliocentric Julian Day time of photometric maximum and E is the cycle count from 2,411,999.693. We obtain phase by solving quadratic Equation (1) for each observed HJD. The fractional part of the solution is the phase, Φ.

2.2. The RV Data

We interpret the failure of the previous parallax determination (Benedict et al. 2007) as due to a nearly face-on orbit for the η Aql AB system. This created degeneracy in the parallax solution between parallactic motion and orbital motion. Without knowledge of the orbit, and only six distinct epochs of astrometry, Benedict et al. (2007) could not determine a perturbation orbit and thus a parallax.

η Aql, known to be a triple system, has a wide companion much too distant from the Cepheid to cause angular motion on a timescale of a few years, the duration of the astrometric observations. High-precision radial velocities of the primary are vital to disentangle the characteristics of the inner system. Cepheid velocity curves repeat very precisely, and techniques have been developed to remove the pulsation velocity from orbital motion with high accuracy (Evans 2000). These techniques have success because the orbital period is typically much longer than the typical Cepheid pulsation period.

Given estimates for the masses of η Aql A and B (5.7 and 2.3 $\mathcal{M}_{\odot}$, Evans et al. 2015) and the absence of any detectable periodic RV variation with amplitude larger than 1 km s^{-1}, to discover and measure the RV variation of the inner binary η Aql AB requires that we determine a very high-quality pulsation curve for η Aql, and measure a time drift in the center-of-mass velocity relative to that curve caused by the orbital motion. With the HET High Resolution Spectrograph (HRS; Tull 1998) and the 2.7 m Harlan J Smith telescope (HJS) coudé spectrograph, both using an iodine cell (Cochran et al. 2004), we should do better than previous ground-based efforts. (We used the 9.2 m HET for its queue-scheduled capability, not its aperture.) The uncertainties in the iodine cell radial velocities are sufficiently small to detect orbital motion on the scale of a few tens of m s^{-1}.

Table 3
Eaton Radial Velocities

TJD[a]	Phase	RV[b]	Error
54,386.6087	0.169800	−26.87	0.10
54,388.6734	0.457487	−15.78	−0.02
54,391.6386	0.870647	−8.52	0.16
54,396.6376	0.567188	−10.13	0.33
54,399.6884	0.992275	−31.76	0.27
…	…	…	…

Notes.
[a] Julian Day − 2,400,000.0.
[b] Relative velocity in km s^{-1}. See Table 5 for correction to absolute velocity.

(This table is available in its entirety in machine-readable form.)

Table 4
Coralie and Hermes Radial Velocities

TJD[a]	Phase	RV[b]	Error	Source[c]
56,096.6778	0.443989	−15.55	0.02	H
56,097.6907	0.585123	−7.74	0.02	H
56,098.6831	0.723398	6.03	0.02	H
56,099.6977	0.864769	−6.77	0.02	H
56,855.5415	0.180871	−25.93	0.02	H
56,856.5404	0.320044	−19.51	0.02	H
…	…	…	…	…

Notes.
[a] Julian Day − 2,400,000.0.
[b] Relative velocity in km s^{-1}. See Table 5 for correction to absolute velocity.
[c] H = Hermes spectrograph on the Mercator Telescope; C = Coralie spectrograph on the Euler Telescope.

(This table is available in its entirety in machine-readable form.)

In a very short integration time of 35 s we typically obtained a signal-to-noise ratio (S/N) of ∼600 pixel^{-1} for the HET.

We received HET-HRS time in four scheduled trimesters, totaling 111 observations over 107 nights in the interval 2010 August 10–2011 November 16. We used the 316g cross-disperser, centered at 5936 Å, with the echelle grating in the "central" position (i.e., on the blaze). The spectrograph was fed with a fiber that subtended 2″ on the sky. We used a spectral resolving power of 60,000 for all of the I$_2$ cell observations.

Table 5
Sources of η Aql Radial Velocities

Key[a]	# RV	γ[b]	Source
Kiss & Vinko	14	-0.68 ± 0.11	Kiss & Vinkó (2000)
Bersier	38	-0.36 ± 0.10	Bersier (2002)
Storm	26	-0.23 ± 0.20	Storm et al. (2004)
TGB05	30	-0.56 ± 0.18	Barnes et al. (2005)
Eaton	217	0.00	Eaton (2020)
HET T1	34	-30.62 ± 0.03	HET, Template 1, this paper
HET T2	36	-30.72 ± 0.04	HET, Template 2, this paper
HET T3	25	-21.50 ± 0.05	HET, Template 3, this paper
HJS T1	25	-21.53 ± 0.08	HJS, Template 1, this paper
HJS T2	26	-4.77 ± 0.09	HJS, Template 2, this paper
Borgniet	13	-0.12 ± 0.14	Borgniet et al. (2019)
Cor & Herm	55	-0.56 ± 0.03	Coralie & Hermes, this paper

Notes.
[a] Legend symbol in Figures 1 and 2.
[b] Velocity offsets required to minimize residuals to a Fourier description of the pulsation velocity of η Aql, assuming an Eaton offset, $\gamma = 0$.

Table 6
Fourier Coefficients Describing the η Aql Pulsational RV Variation

j	a	σ_a	b	σ_b
0	-15.328	0.021	0.000	0.000
1	-7.389	0.019	-13.510	0.016
2	-7.876	0.019	-1.626	0.016
3	-1.916	0.018	2.445	0.017
4	-0.344	0.017	1.394	0.018
5	0.794	0.015	0.467	0.020
6	0.250	0.015	0.024	0.019
7	0.088	0.014	-0.160	0.020
8	-0.085	0.016	-0.003	0.017
9	-0.134	0.016	0.026	0.017
10	-0.082	0.016	0.015	0.016
11	0.025	0.016	0.079	0.016
12	0.067	0.015	0.017	0.016

The observing sequence included the standard calibration frames shared by all programs using a given HET-HRS configuration: five bias frames, 11 flats without the I_2 cell, three flats with the I_2 cell, and one or two Th–Ar frames for wavelength calibration, and then one frame for η Aql with the I_2 cell at some time during the night. On three different nights we observed η Aql at high signal-to-noise ratio at a resolving power of 120,000 with and without the I_2 cell to obtain a stellar "template" spectrum for the high-precision radial velocity computation. These template spectra were obtained at pulsation phases of 0.39265, 0.65822, and 0.21875. Thus, they sample very different phases of the pulsation cycle.

Observations with the McDonald Observatory 2.7 m Harlan J Smith Telescope were obtained using the Tull coudé spectrograph (Tull et al. 1995). This instrument is a cross-dispersed white-pupil echelle spectrograph covering 3750–10200 Å. A 1″2 entrance slit gave a spectral resolving power of 60,000. We used a temperature-controlled I_2 vapor absorption cell in front of the spectrograph slit to provide extremely stable wavelength calibration and to enable excellent reconstruction of the instrumental profile.

We obtained a total of 50 spectra of η Aql with the HJS Tull Spectrograph and I_2 cell between 2018 September 15 and 2019 September 30. We also obtained spectra of η Aql without the I_2 cell on two separate nights for template spectra for the precise radial velocity calculations. These were obtained at η Aql pulsation phases of 0.07198 and 0.39497. A 50 s integration with the HJS Tull coudé spectrograph gives S/N of $\sim$300 pixel^{-1}.

2.3. HET and HJS Data

The data from each night of HET and HJS observations were reduced separately. We used automated scripts of IRAF tasks to perform standard bias removal, scattered light removal, and flat-fielding of the data frames. The apertures for each echelle spectral order were traced, and the spectra were extracted. Wavelength calibration was obtained from the Th–Ar hollow-cathode lamp spectra. Since the HET-HRS did not contain an exposure meter, the mid-exposure time was estimated to be halfway between the exposure start and stop times. The HJS Tull spectrograph does contain an exposure meter, which records the relative flux passing through the entrance slit in 1 s intervals as a function of time. We used this time series to compute the barycentric correction for each time interval of the exposure meter according to the procedure of Wright & Eastman (2014). We then weighted each of these by the exposure meter flux to compute the flux-weighted barycentric correction for the exposure.

Our primary goal is to establish an RV orbit for the perturbation caused by the B9.8V companion, and to incorporate that orbit into the astrometric analysis, permitting a determination of both a parallax and a companion mass. We first model the RV variation due to Cepheid pulsation, then search for RV variation (an orbit) in the residuals to that determination. We computed radial velocities from the observed HET and HJS spectra using a method very similar to that described by Marcy & Butler (1992). The radial velocity code computes the shift of the template spectrum relative to the I_2 spectrum that is needed to match the observed program spectrum, after convolution with the model instrumental profile, as defined primarily by the observed shape of the superimposed I_2 absorption lines. The "radial velocity" computed is just $c \times \delta\lambda/\lambda$ where $\delta\lambda$ is the observed spectral shift. The apparent RV variations due to the Cepheid pulsation result from the time variations in the overall photospheric velocity field due to the star's periodic expansion and contraction, rather from true center-of-mass motions of the star.

The stellar line profiles undergo significant changes in shape through the Cepheid pulsation cycle. Indeed, lines formed at different depths in the atmosphere will exhibit different patterns of profile variation. The "radial velocity" measurement process basically computes the first moment of the mean stellar absorption line profile. For a nonpulsating and inactive star, this would be an excellent approximation to its center-of-mass motion. Since the different template spectra were obtained at different Cepheid pulsation phases, they have different stellar line profile shapes. Thus, one might expect subtle variations in the RV curves computed with the different templates. The HET template with quadratic phase, $\Phi = 0.39$, yielded velocities with smaller internal errors, possibly because of proximity in phase to structure in the pulsational RV (e.g., Figure 1). Superimposed on these line profile variations is the true RV orbital motion of stellar components A and B. Our recent HET velocities are given in Table 1, along with phases calculated from Equation (1), and template identification. Our
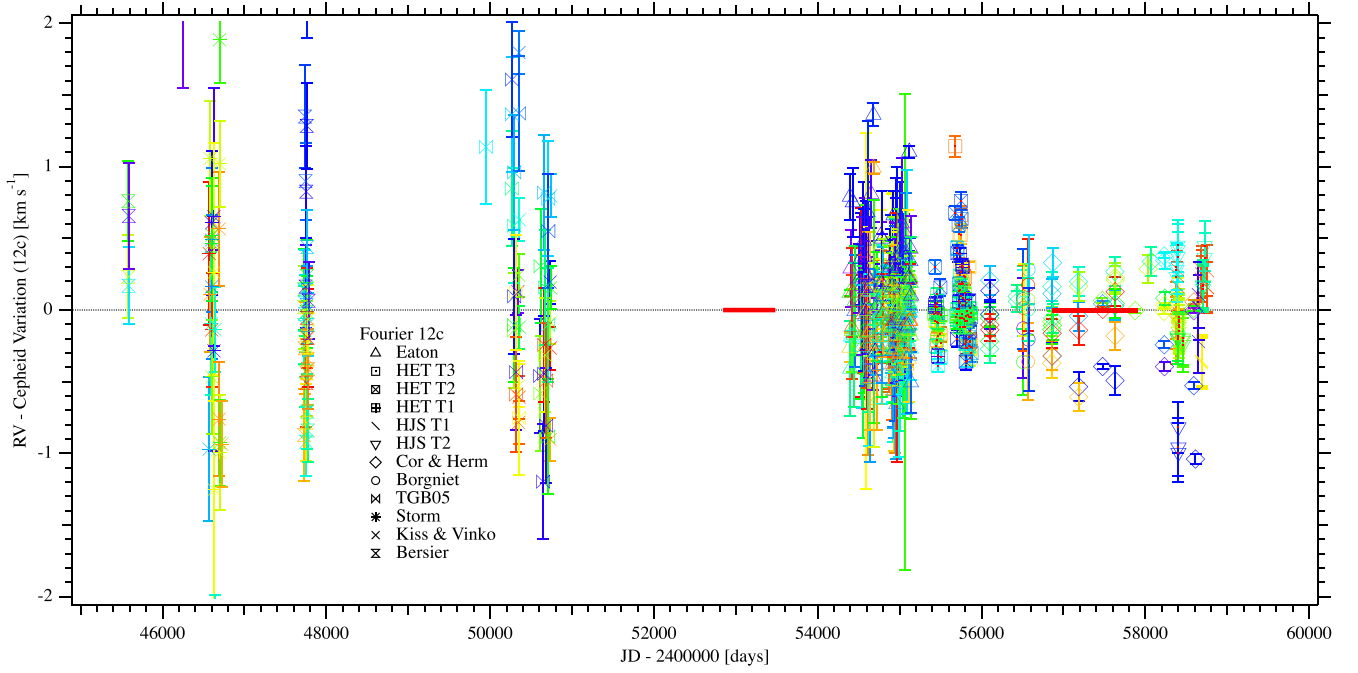
Figure 2. Residuals (Figure 1, top) to the pulsation-induced RV, modeled by the Fourier coefficients listed in Table 6 plotted as a function of time for the sources listed in Table 5. Errors come from Tables 1–4 and the various published sources in Table 5. RV values are color-coded by Cepheid phase as for Figure 1 (red = 0 to blue = 1). The solid red bars on the zero RV line indicate astrometric coverage from HST/FGS (left) and Gaia EDR3 (right).
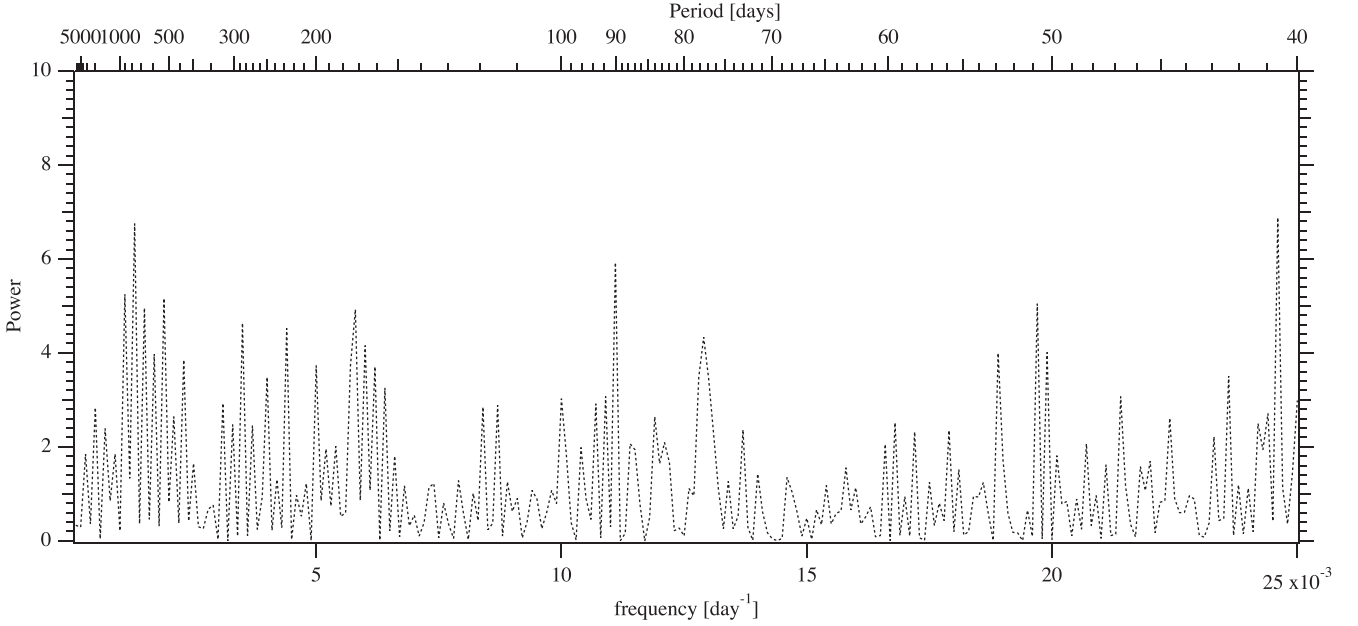

Figure 3. Lomb–Scargle periodogram of RV in Figure 2. No peak indicates a false alarm probability less than 61%. The minimum frequency range (maximum period) explored corresponds to roughly 2/3 the total time span of the RV data.

recent HJS velocities are given in Table 2, along with phases calculated from Equation (1), and template identification.

2.4. Other RV Data

We also had access to 217 radial velocities of η Aql from the 2 m Tennessee State University Automatic Spectroscopic Telescope (Eaton & Williamson 2007; Eaton 2020) obtained over a period of two years: late 2007 to late 2009. Table 3 contains the Eaton (2020) velocities kindly sent in advance of

publication. Table 4 contains an additional unpublished 55 high-precision RVs from the Hermes spectrograph on the Mercator Telescope (La Palma) and from the "Coralie" spectrograph on the Euler Telescope at La Silla. See Anderson et al. (2016) for an example of reduction details.

2.5. Fourier Decomposition of Pulsation-induced RV

We seek to minimize residuals to a description RV = f(phase) of the observed RV variation derived from

Table 7
Gaia EDR3 Astrometry Priors[a]

ID	EDR3 ID	ϖ	μ_α	μ_δ	RUWE	G
		η Aql				
1	Gaia EDR3 4240272953377646592	3.67 ± 0.19	8.89 ± 0.18	-8.32 ± 0.14	2.561	3.748 ± 0.014
2	Gaia EDR3 4240273159535375104	0.24 0.01	-3.73 0.02	-4.38 0.01	1.049	13.258 0.003
3	Gaia EDR3 4240272334901581184	0.84 0.03	-9.28 0.03	-3.90 0.03	1.023	15.242 0.003
4	Gaia EDR3 4240272644139211904	0.19 0.03	-0.88 0.03	-3.44 0.02	0.952	15.188 0.003
6	Gaia EDR3 4240272781578178048	0.45 0.02	-2.74 0.02	-11.40 0.02	1.02	14.250 0.003
		ζ Gem				
1	Gaia EDR3 3366754155291545344	3.07 ± 0.22	-7.74 ± 0.25	-0.94 ± 0.17	2.778	3.540 ± 0.006
2	Gaia EDR3 3366753296297433984	0.37 0.02	-0.86 0.02	-2.71 0.01	0.979	13.589 0.003
5	Gaia EDR3 3366795558775643904	1.26 0.04	-4.83 0.05	-7.39 0.03	2.170	12.267 0.003
8	Gaia EDR3 3366754464528540416	28.64 0.02	-81.97 0.03	41.33 0.02	0.848	7.432 0.003
10	Gaia EDR3 3366754086571429376	0.48 0.02	2.19 0.02	-0.03 0.02	1.036	14.291 0.003
11	Gaia EDR3 3366754395807337600	0.57 0.01	4.16 0.01	-4.49 0.01	1.027	12.336 0.003

Note.
[a] Units are: ϖ, mas; μ_α, μ_δ, mas yr^{-1}. In each field ID = 1 denotes the Cepheid.

Fourier coefficients (Evans et al. 2015). We use GaussFit (Jefferys et al. 1988) with these equations of condition:

$$\text{RVC} = V(\text{Phase}) - V(\text{obs}) - \gamma(S) \quad (2)$$

and

$$V(\text{Phase}) = \gamma(S) + \sum_{j=1}^{N}(a[j] \times \cos(j \times z) + b[j] \times \sin(j \times z)) \quad (3)$$

where RVC is the Cepheid pulsation signature; V(Phase) is calculated from the Fourier coefficients, a and b; $z = 2\pi \times$ Phase; V(obs) are the measured velocities from each source; and $\gamma(S)$ is a velocity offset that depends on the RV source (listed in Table 5). We modeled the velocities (sources in Table 5) with $N = 6$, 10, 12, and 14 coefficients and found a χ^2 minimum at 12 coefficients. We list the coefficients with error estimates in Table 6. Figure 1 contains (top) the residuals from a modeling of pulsational RV with 12 coefficients for all the RV sources listed in Table 5, and (bottom) all velocities corrected for the γ offsets listed in Table 5.

2.6. No RV Perturbation Orbit

Once the RV signature due to pulsation has been removed, we are left with the residuals to the Fourier fits to the various velocity sources in Table 5. We search these for a perturbation caused by the B9.8V companion. Figure 2 plots those residuals against TJD. Even though the average internal errors for many of the investigations in Table 5 are small, we note quite large scatter in the residuals for all data sets. We ascribe this scatter to the assumption in the RV computation processes that the stellar line profiles do not change with time. Visual inspection fails to provide any obvious RV variation due to orbital motion. Figure 3 shows a Lomb–Scargle periodogram of the RV residuals from the top of Figure 1. The lack of any significant peak at any of the probed periods implies either a nearly face-on orbit with an as yet unknown period or a period significantly longer than those probed in Figure 3.

3. HST/FGS Astrometry

An absolute K-band magnitude for η Aql is a major goal of the present investigation. To place η Aql (with $\log P = 0.85592$)

exactly on the Benedict et al. (2007) LL requires a K-band absolute magnitude (with absorption, $A_K = 0.05$ mag), $M_K = -5.23$. This in turn requires a parallax $\varpi_{\text{abs}} = 3.77$ mas with no Lutz–Kelker–Hanson (LKH) bias correction.[5] Benedict et al. (2007) were unable to derive an η Aql parallax consistent with that LL. At that time we blamed this failure on an unmodeled orbital perturbation due to the B9.8V companion, η Aql B. We now revisit the η Aql astrometry, and to validate our newer astrometric modeling and explore the odd behavior of η Aql, we use another Cepheid, ζ Gem with $\log P = 1.00649$, as a control sample. The EDR3 parallax of ζ Gem (Table 7) yields (assuming the Benedict et al. 2007 $A_K = 0.02$) $M_K = -5.60 \pm 0.15$ mag, in agreement with the Benedict et al. (2007) prediction for that $\log P$, $M_K = -5.73$.

3.1. The Astrometric Data

For η Aql the astrometric data consist of ten discrete sets containing a total of 111 positions: 37 of η Aql and 74 for four reference stars, all secured with FGS 1. One entire set of η Aql observations was discarded because of anomalously large residuals. Inspection of the processed data indicated poor drift correction[6] due to excessive spacecraft motion. The average positional error of the reference star in y has a typical value of 2.6 mas. For this field the average error of the reference star in x has an atypical value, 6.2 mas. The ζ Gem data consist of 11 discrete sets containing 201 positions: 51 of ζ Gem and 150 for five reference stars. In contrast to η Aql, the ζ Gem field (Benedict et al. 2007) has average x and y errors for the reference star of 2.4 and 3.7 mas, respectively. Relative positions of the astrometric reference stars are plotted in Figure 4, with Gaia EDR3 identifications; parallaxes, ϖ; proper motions, μ_α, μ_δ; and G magnitudes listed in Table 7. At each epoch we measured each reference star 1–3 times and the Cepheid 3–4 times.

3.1.1. Modeling Priors

The success of single-field parallax astrometry depends on prior knowledge of the reference stars, and sometimes, but less

---

5 Once a measured parallax exists we apply the LKH correction, explained in Section 5 of Benedict et al. (2007).
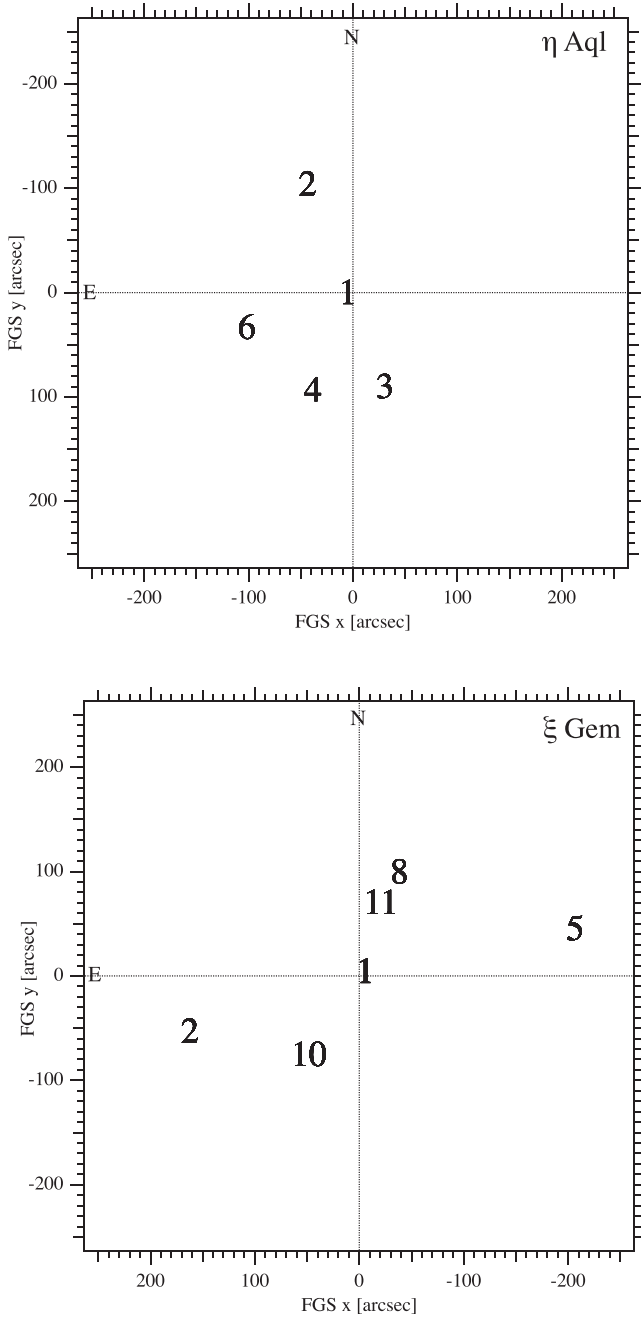6 See Benedict et al. (1998), Section 3.3.2.

Figure 4. Top: relative positions of η Aql (1, center) and the astrometric reference stars (2, 3, 4, 6). Bottom: relative positions of ζ Gem (1, center) and the astrometric reference stars (2, 5, 8, 10, 11). Table 7 identifies each reference star.

ideally, of the science target. Catalog proper motions with associated errors, lateral color corrections, and estimates for reference star parallax are entered into the modeling as quasi-Bayesian priors, data with which to inform the final solved-for parameters. These values are not entered as hardwired quantities known to infinite precision. We include them as observations with associated errors. The model adjusts the corresponding parameter values within limits defined by the data input errors to minimize χ^2, yielding the most accurate parallax and proper motion for each Cepheid, and in the case of η Aql, the best opportunity to measure any reflex motion due to the companion, η Aql B. We list the various priors below.

1. *Absolute Parallaxes of Reference Stars.* Because we measure the parallax of a Cepheid with respect to reference stars that have their own parallaxes, we require estimates of the absolute parallaxes of the stars in the reference frame. For past investigations, (e.g., Benedict et al. 2017, Section 4.1.1), the colors, spectral type, and luminosity class of a star were used to estimate a spectrophotometric parallax, absolute magnitude, M_V, and V-band absorption, A_V. Our task becomes significantly simpler, thanks to Gaia. The Gaia Early Data Release 3 (EDR3) catalog (Gaia Collaboration et al. 2021; Lindegren et al. 2021) provides the necessary parallax information on reference stars with precision and accuracy far superior to that provided by our past methodology for determination. Table 7 lists the parallax priors used in our modeling, along with Gaia EDR3 ID numbers, Gaia G magnitudes, and the renormalized unit weight error (RUWE) for η Aql, ζ Gem, and each reference star. Stassun & Torres (2021) find that the Gaia RUWE robustly predicts unmodeled photocenter motion, even in the nominal "good" range of 1.0–1.4 (see also Belokurov et al. 2020). RUWE values for reference stars (Table 7) suggest clean reference frames with the η Aql set of reference stars slightly better. The average parallax error of reference stars is $\langle \varpi \rangle = 0.02$ mas.

2. *Proper Motions.* We use proper motion priors from the EDR3 with errors of the order of 0.05 mas yr^{-1}.

3. *Lateral Color and Cross-filter Corrections.* These are necessary because the FGS contains refractive optics, and a neutral density filter required to observe η Aql, $V = 3.9$, ζ Gem, $V = 3.8$, and reference star #8 for ζ Gem with $V = 7.55$. We use values for those priors from Benedict et al. (2007). We list $B - V$ colors used for the lateral color correction in Table 8, which, for completeness, also contains near-IR colors from the Two Micron All Sky Survey (2MASS).

4. *Cepheid $(B - V)$ versus Phase.* Cepheids exhibit substantial changes in $(B - V)$ color index as a function of phase, with $\Delta(B - V) \simeq 0.6$ mag for η Aql and $\Delta(B - V) \simeq 0.3$ for ζ Gem. To ensure the best possible astrometric results in the presence of a lateral color effect, we model sets of $(B - V)$ (Engle 2015 for η Aql; Moffett & Barnes 1980; Berdnikov 2008, for ζ Gem) with a fifth-order polynomial (Figure 5) to predict $(B - V)$ at each epoch of FGS observation. We list the polynomial coefficients in Table 9.

3.2. The Astrometric Model

From positional measurements we determine for each observation set rotation, scale, and offset parameters relative to an arbitrarily adopted constraint epoch. We employ GaussFit (Jefferys et al. 1988) to minimize χ^2. The solved equations of the condition are:

$$x' = x + lc_x(B - V) \tag{4}$$

$$y' = y + lc_y(B - V) \tag{5}$$

$$\xi = Ax' + By' + C - \mu_\alpha \Delta t - P_\alpha \varpi \ [-\Delta XFx] \tag{6}$$

$$\eta = Dx' + Ey' + F - \mu_\delta \Delta t - P_\delta \varpi \ [-\Delta XFy]. \tag{7}$$

Identifying terms, x and y are the measured coordinates from HST; $(B - V)$ is the Johnson $(B - V)$ color of each star
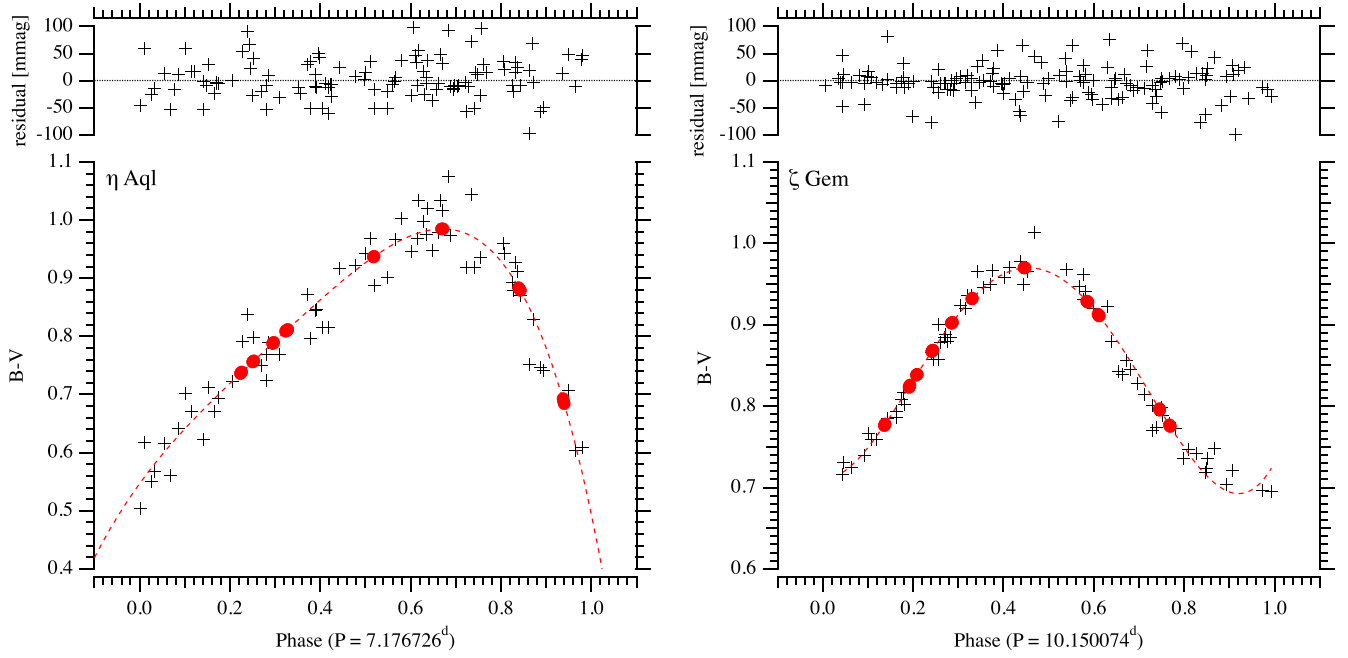
Figure 5. $B - V$ variation as a function of phase. Fit is the fifth-order polynomial listed in Table 9. The red dots indicate phases at which we secured FGS astrometry. This fit provides the $B - V$ values used for η Aql and ζ Gem in Equations (4) and (5).

Table 8
Visible and Near-IR[a] Photometry

ID	V	$B - V$	K	$J - H$	$J - K$	$V - K$
			η Aql			
1	3.91 —		1.98 0.01	0.40 0.01	0.48 0.01	1.93 —
2	13.68 0.03	1.53 0.03	10.142 0.025	0.796 0.033	0.927 0.036	3.778 0.04
3	15.25 0.03	0.75 0.05	13.453 0.031	0.454 0.046	0.449 0.048	1.847 0.04
4	15.31 0.03	1.13 0.04	12.919 0.035	0.529 0.040	0.629 0.045	2.451 0.05
6	14.40 0.03	1.02 0.05	11.905 0.026	0.629 0.036	0.706 0.034	2.645 0.04
			ζ Gem			
1	3.79 —		2.182 0.288	0.401 0.359	0.257 0.387	1.858 —
2	13.78 0.06	1.74 0.1	11.537 0.018	0.567 0.033	0.614 0.028	2.303 0.06
5	12.36 0.03	0.74 0.06	11.103 0.020	0.307 0.030	0.331 0.028	1.267 0.04
8	7.55 0.02	0.69 0.05	6.108 0.023	0.366 0.028	0.373 0.030	1.452 0.03
10	14.25 0.02	0.61 0.04	13.127 0.032	0.302 0.044	0.348 0.041	1.203 0.04
11[b]	12.56 0.03	0.66 0.1	…	…	…	…

Notes.
[a] Sources: for η Aql and ζ Gem (ID = 1), Barnes et al. (1997); Welch et al. (1984); for reference stars (ID = 2–6, ID = 2–11), 2MASS (Skrutskie et al. 2006) and sources discussed in Benedict et al. (2007).
[b] Star too close to ζ Gem for 2MASS measurement.

(Table 8); and lc_x and lc_y are the lateral color corrections. A, B, D, and E are scale and rotation plate parameters, C and F are offsets; μ_α and μ_δ are proper motions; Δt is the time difference from the constraint epoch; P_α and P_δ are parallax factors; and ϖ is the parallax. We obtain the parallax factors from a JPL Earth orbit predictor (Standish 1990), version DE405. ΔXFx and ΔXFy are the cross-filter corrections in x and y. The terms in square brackets, $[\cdots]$, are determined only by the Cepheid, and in the case of ζ Gem, the bright reference star #8.

3.3. Four Applications of the Model

Carrying out the following analyses for both Cepheids, we first use their associated reference stars with Gaia EDR3 parallax and proper motion priors (from Table 7) to model scale, rotation, offsets, and individual reference star parallax and proper motion values required to transform the separate observation epochs onto the Gaia reference frame (Step 1). We next apply the derived scale, rotation, and offset values to the Cepheid FGS observations, deriving only Cepheid parallax and proper motion (Step 2). Step 3 involves re-deriving scale, rotation, and offset values, and reference star and Cepheid parallax and proper motion, allowing the Cepheid astrometry to inform the scale, rotation, and offset values. Neither Step 2 nor Step 3 incorporates Gaia EDR3 priors for η Aql or ζ Gem. Step 4 repeats Step 3, this time introducing Gaia EDR3 parallax and proper motion priors for each Cepheid. In each of Steps 2–4 we compare our derived Cepheid parallax and proper motion with the EDR3 values listed in Table 7.

Table 9
$B - V$[a] as a Fifth-order Polynomial Function of Phase

Term	Value	Error
	η Aql	
K0	0.5468	0.0226
K1	1.0729	0.332
K2	−1.6424	1.41
K3	3.553	2.19
K4	−3.0371	1.11
	ζ Gem	
K0	0.7102	0.0150
K1	−0.0111	0.1871
K2	5.0592	0.7227
K3	−11.0439	1.0546
K4	6.0166	0.5133

Note.
[a] Figure 5.

Table 10
Reference Frame Statistics

Parameter	Value
η Aql	
Study duration	1.74 yr
Number of observation sets	10
Reference star average V	14.66
Reference star average $(B - V)$	1.11
Field A_K	0.05 mag
x residual rms	1.1 mas
y residual rms	0.8 mas
ζ Gem	
Study duration	1.50 yr
Number of observation sets	11
Reference star average V	12.03
Reference star average $(B - V)$	0.69
Field A_K	0.00 mag
x residual rms	1.3 mas
y residual rms	1.2 mas

3.3.1. Step 1: Model the Reference Stars

This step assesses the overall quality of the FGS astrometry. The optical field angle distortion (OFAD) calibration (McArthur et al. 2002) reduces as-built HST and FGS 1r distortions with magnitude from ∼1″ to below 2 mas over much of the FGS 1r field of view. From histograms of the FGS astrometric residuals obtained via Equations (4)–(7) (Figure 6) we conclude that we have well-behaved reference star solutions exhibiting residuals with Gaussian distributions with dispersions $\sigma \leqslant 1.0$ mas. We determine the η Aql field reference frame "catalog" for FGS 1r in ξ and η standard coordinates with average uncertainties, $\langle \sigma_\xi \rangle = 1.2$ and $\langle \sigma_\eta \rangle = 0.5$ mas, again indicating poorer performance along the FGS 1r x-axis. The rms values for x and y residuals are 1.1 and 0.8 mas. Surprisingly, many of the larger residuals come from reference star 4, which has the lowest RUWE value (Table 7). The ζ Gem field reference frame "catalog" for FGS 1r in ξ and η standard coordinates has average uncertainties, $\langle \sigma_\xi \rangle = 0.6$ and $\langle \sigma_\eta \rangle = 0.4$ mas. For ζ Gem the rms values for x and y residuals are 1.3 and 1.2 mas. We present reference frame statistics in Table 10. In Figure 7 we plot the reference star residuals as a function of time. Neither the η Aql nor the ζ Gem reference frame exhibits obvious patterns.

3.3.2. Step 2: Determine Cepheid Parallax and Proper Motion

Once we have determined plate parameters A through F, using only reference star astrometry, they become plate constants in Equations (4)–(7) for modeling, which now includes, in turn, the astrometric measurements for each Cepheid. In other words, we rotate, scale, and offset the original Cepheid position measurements into the reference frame defined by their respective reference stars, while solving for Cepheid parallax and proper motion. This model does not include parallax and proper motion priors for the Cepheids. We list these results in Table 11, and display the resulting η Aql and ζ Gem residuals against TJD in Figure 8. The η Aql residuals slightly exceed those for ζ Gem. Note the significant parallax mismatch for η Aql compared to the EDR3 value in Table 7, and that the ζ Gem parallax agrees almost perfectly with EDR3.

3.3.3. Step 3: Cepheid Measurements Contribute to Reference Frame Model while Re-determining Cepheid Parallax and Proper Motion

For this step the data used to establish coefficients A–F in Step 1 now include the Cepheid positional measurements, but without EDR3 parallax and proper motion priors for the Cepheids. We display the resulting η Aql and ζ Gem residuals against TJD in Figures 9 and 10, along with their corresponding reference star residuals. Note the striking reduction in η Aql residuals compared to the result of Step 2 (Figure 8), which is at the expense of inflating (compared to Figure 7) the reference star residuals. This model includes neither parallax nor proper motion priors for the Cepheids, and yields the parallax and proper motion values listed in Table 12, which for comparison also includes the Benedict et al. (2007) results for ζ Gem. The η Aql parallax remains significantly different from the EDR3 value, while the ζ Gem parallax continues to agree within the errors with both the EDR3 and Benedict et al. (2007) values.

3.3.4. Step 4: Re-determine Cepheid Parallax and Proper Motion with Strong EDR3 Priors

Figures 11, 12 and Table 13 show the results of including the very restrictive EDR3 priors for parallax and proper motion, again allowing Cepheid astrometry to assist in determining A–F. Basically, the FGS parallaxes of η Aql and ζ Gem are consistent with the Gaia values, but for η Aql only, by further increasing the η Aql reference star residual rms. These models produce parallaxes and proper motions that are essentially the input priors, but have decreased the formal errors of the Gaia EDR3 parallax and proper motion by factors of 2–3. A future, similar reprocessing of the other Benedict et al. (2007) Cepheids might improve the LL in Figure 13.

4. Discussion

We first review our derived ζ Gem and η Aql parallaxes, then discuss possible causes for the large η Aql astrometric residuals obtained from Step 2 (Section 3.3.2). Ascribing the increase in η Aql residual to AB system orbital motion, and assuming a mass range for the B component from the literature, we
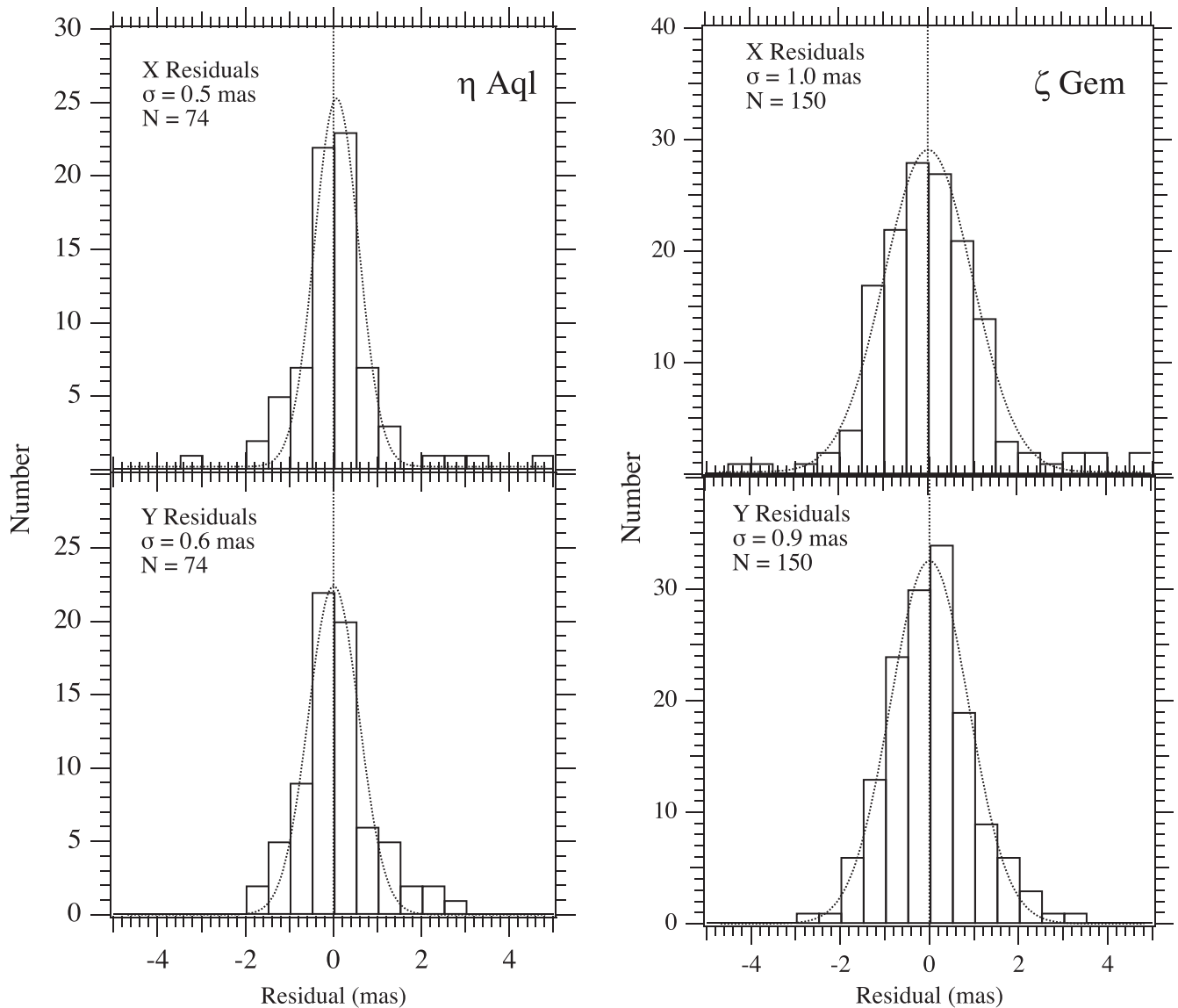
Figure 6. Results from Step 1. Histograms of *x* and *y* residuals obtained from modeling the FGS observations of each FGS reference frame (for η Aql stars 2, 3, 4, 6; for ζ Gem stars 2, 5, 8, 10, 11; in Figure 4) with Equations (2)–(5). Distributions are fit with Gaussians with standard deviations, σ, indicated in each panel. In addition to fewer reference stars, one entire set of η Aql observations was discarded due to anomalously large residuals.

estimate possible orbital periods and separations. Next, we hypothesize that the difference in η Aql parallax between that measured in Step 2 and that predicted from the Benedict et al. (2007) LL might result from an A–B system period near one year. Lastly, we investigate the possibility that the observed image motion is purely a result of the variability of η Aql.

4.1. Parallax Results

We first review the unsurprising ζ Gem parallax results. No matter what the input priors, the models in Steps 2–4 yield parallax values (Tables 11–13) that all agree within their respective errors, both with the Benedict et al. (2007) value and with EDR3. We interpret this as a validation of our modeling approach.

From Step 2, as reported in Table 11, applying *A–F* in Equations (4)–(7) as plate constants to the measurements of η Aql, including no EDR3 priors, we obtain a parallax and *K*-band absolute magnitude that place η Aql over one

magnitude below the LL determined in Benedict et al. (2007). This model also results in the large η Aql residuals seen in Figure 8. Step 3, allowing the η Aql measurements to contribute to determining *A–F* in Equations (4)–(7), while solving for parallax and proper motion, provides no resolution to the parallax disagreement, but does significantly reduce the η Aql residuals, while increasing the reference star residual rms, demonstrating the malleability of the reference frame. Step 4 finally yields a parallax in agreement with EDR3, and that the η Aql reference frame flexes in response to strong Cepheid priors.

η Aql A pulsates as a fundamental-mode Cepheid with a well-known period. Astrophysical explanations for why it would have an absolute *K*-band magnitude more than one magnitude lower than predicted by the Benedict et al. (2007) LL (Figure 13) do not readily spring to mind. However, could the companion, η Aql B, produce a perturbation that could change a measured parallax?
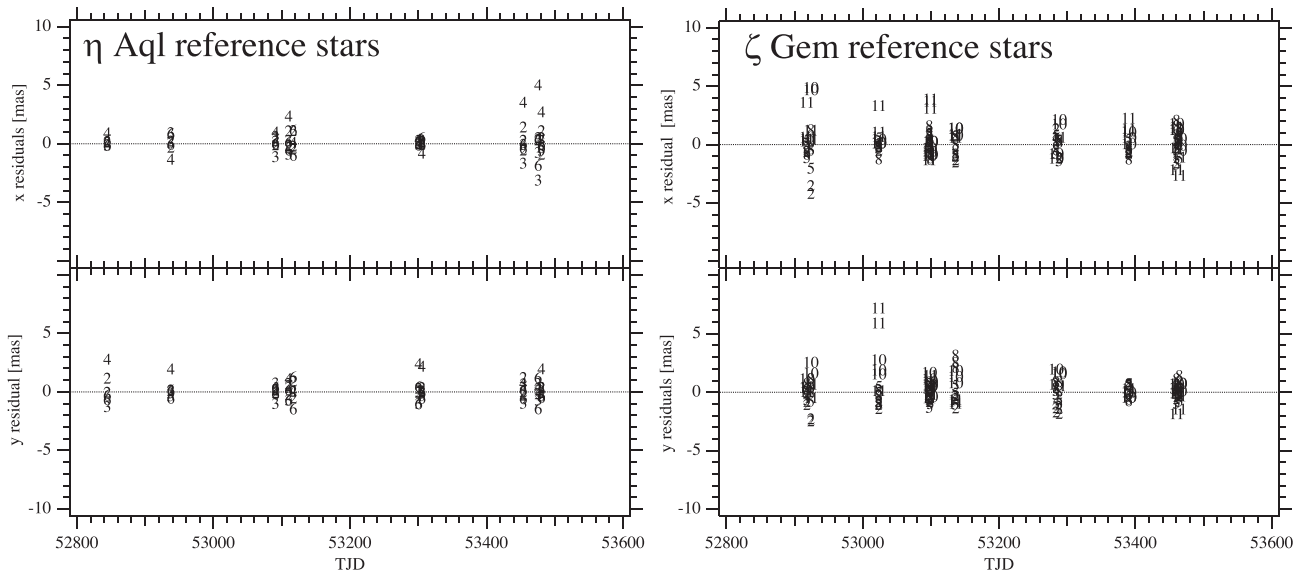
Figure 7. Results from Step 1. Reference star position residuals from the model of Equations (4)–(7) plotted against TJD for the η Aql and ζ Gem fields. We identify reference stars by Table 7 ID number. Because there are outliers, the equivalent (x, y) rms values have values of 1.1 and 0.8 mas for η Aql, and 1.3 and 1.2 mas for ζ Gem, all larger than the 1σ standard deviations of the Gaussian distribution in Figure 6 for these same residuals.

Table 11
Step 2: Cepheid Parallax, Proper Motion, and Absolute Magnitude

Parameter	Value
η Aql	
ϖ	6.55 ± 0.25 mas
μ_α	7.19 ± 0.25 mas yr^{-1}
μ_δ	-7.50 ± 0.27 mas yr^{-1}
$\boldsymbol{\mu}$	10.39 mas yr^{-1}
P.A.	136°2
LKH corr.	-0.01 mag
Field A_K	0.05 mag
$(m - M)_0$	5.97 mag
M_K	-4.01 ± 0.08 mag
ζ Gem	
ϖ	3.00 ± 0.32 mas
μ_α	-7.51 ± 0.49 mas yr^{-1}
μ_δ	-0.19 ± 0.29 mas yr^{-1}
$\boldsymbol{\mu}$	7.51 mas yr^{-1}
P.A.	268°6
LKH corr.	-0.09 mag
field A_K	0.02 mag
$(m - M)_0$	7.70 mag
M_K	-5.71 ± 0.23 mag

Alternatively, there are a number of differences between the η Aql and ζ Gem astrometry that might combine to explain the discrepant η Aql parallax: there are only four reference stars for η Aql as opposed to five for ζ Gem; there are 18 observations per reference star for η Aql and 30 observations per reference star for ζ Gem; there are 37 positional measurements of η Aql as opposed to 51 for ζ Gem; there is an additional epoch for ζ Gem; the error along the FGS x-axis is 6.2 mas for η Aql, nearly twice that for ζ Gem. Despite all those differences, both η Aql and ζ Gem exhibit similar levels of structure in the residuals shown in Figure 8.

FGS astrometry of one previous parallax target also yielded parallax in poor agreement with other determinations. Benedict et al. (2011) investigated the Population II Cepheid, VY Pyx,

finding a parallax, $\varpi = 6.44 \pm 0.23$ mas, placing it +1.19 magnitude below a period–luminosity relation defined by five RR Lyr stars and one other Population II Cepheid, κ Pavonis (see Figure 3 in Benedict et al. 2017). VY Pyx, with a very clean RUWE = 0.89 value, has a Gaia EDR3 $\varpi = 3.95 \pm 0.02$ mas, placing it on the Benedict et al. (2011) period–luminosity relation. We proceed on the assumption that whatever unknown pathology afflicted the VY Pyx data did not similarly impact these η Aql measurements.

4.2. Searching for η Aql B

Concerning the η Aql residuals in Step 2 (Figure 8, left), could they be evidence of orbital motion? We assert that they are not evidence of modeling issues, given the consistent ζ Gem parallax results and the near equality of residual rms values for both η Aql and ζ Gem at each step.

Does Gaia provide evidence of anomalous astrometric motion? The Gaia RUWE parameter correlates with photocenter motion (Stassun & Torres 2021). If η Aql B and η Aql A are a dynamical system, then one might expect an RUWE value larger than $\sim$1.4. Gaia EDR3 catalogs RUWE = 2.6 for η Aql, consistent with astrometric motion. However, for ζ Gem, a Cepheid with no known companion, RUWE = 2.8. The average RUWE value for the ten Cepheids studied in Benedict et al. (2007) is $\langle$RUWE$\rangle = 2.8$. It is unlikely all these Cepheids have astrometrically detectable companions. We ascribe the high RUWE values to a combination of photometric variability and the fact that these Cepheids all have $G < 6$, a brightness limit below which special and experimental position extraction is required.

We now have access to a second indicator of potential orbital motion, the Brandt (2021) χ^2 value. This parameter measures the likelihood of acceleration obtained by comparing proper motion from an earlier epoch from Hipparcos with a Gaia EDR3 proper motion. A larger χ^2 value indicates more significant change (acceleration) in proper motion, thus a higher probability of a perturbing companion. The χ^2 values for the Cepheids W Sgr and FF Aql, both confirmed binaries,
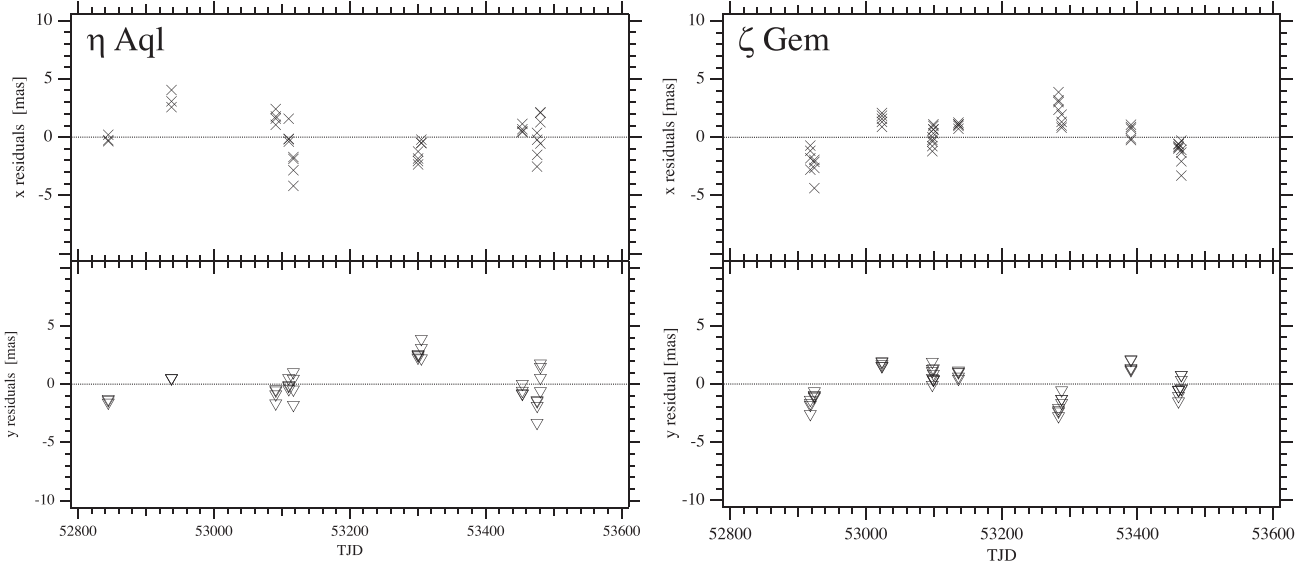
Figure 8. Results from Step 2. Cepheid position residuals plotted against TJD, after applying the coefficients *A*–*F* from Equations (4)–(7) while solving for Cepheid parallax and proper motion. Large residuals suggest unmodeled *η* Aql motion, with rms residuals for *η* Aql (*x*, *y*) = (1.8, 1.6 mas). *ζ* Gem, with no known companion, has rms residuals (*x*, *y*) = (1.7, 1.4 mas).
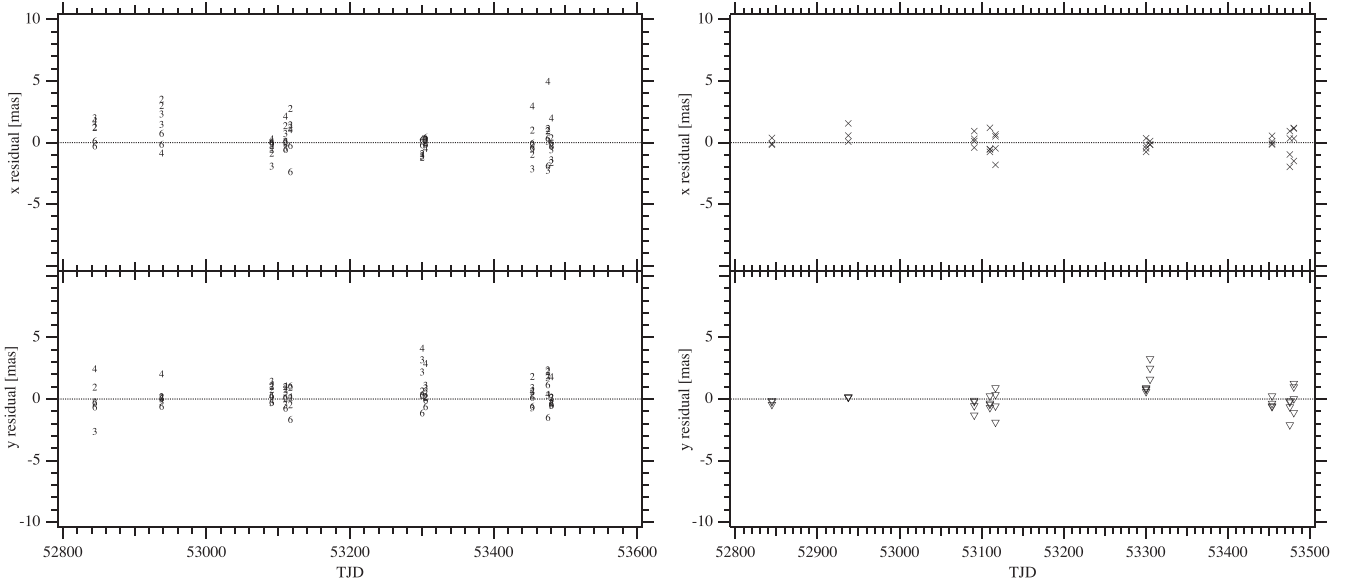

Figure 9. *η* Aql results from Step 3. Right: *η* Aql position residuals plotted against TJD, re-determining coefficients *A*–*F* in Equations (4)–(7) while solving for *η* Aql parallax and proper motion. Compared to Figure 8, allowing *η* Aql to assist in determining *A*–*F* has significantly reduced the *η* Aql rms residuals from (*x*, *y*) = (1.8, 1.6 mas) to (0.8, 1.0 mas). Left: reference star residuals. Compared to Figure 7, including the *η* Aql measurements has increased the reference star residuals rms from (*x*, *y*) = (1.1, 0.8 mas) to (1.4, 1.2 mas). These model inputs yield an *η* Aql parallax, $\varpi = 6.55 \pm 0.25$ mas, which significantly differs from the Gaia EDR3 value, $\varpi = 3.67 \pm 0.19$ mas.

are 6.03 and 129.2. For *η* Aql, $\chi^2 = 0.57$, the lowest of any in the Benedict et al. (2007) Cepheid list. For *ζ* Gem, $\chi^2 = 1.43$. For VY Pyx, our example of previous discrepancy with Gaia, $\chi^2 = 6.70$, which is marginally indicative of unmodeled acceleration.

The question remains; do the relatively large *η* Aql residuals seen in Figure 8 indicate unmodeled orbital motion? They do indicate excess motion, when compared to the reference star residuals in Figure 7, which are relatively flat-line. Comparing *η* Aql residual rms with reference star residual rms, something perturbs *η* Aql A by 0.7–0.8 mas, depending on the axis. As a working hypothesis we assume component B contributes to

photocenter motion, thus to the large astrometric residuals. We identify two possible sources of photocenter motion: orbital and photometric.

4.3. Photocenter Motion Connected to AB Orbit: Mass and Period Limits for *η* Aql B

The RV results yield no period information. They argue for an *η* Aql A–B orbit very close to face-on, or for a very long orbital period. In an effort to further constrain information about *η* Aql B we devise and test two hypotheses, assuming a short period: (i) that *η* Aql B causes the excess *η* Aql A residual
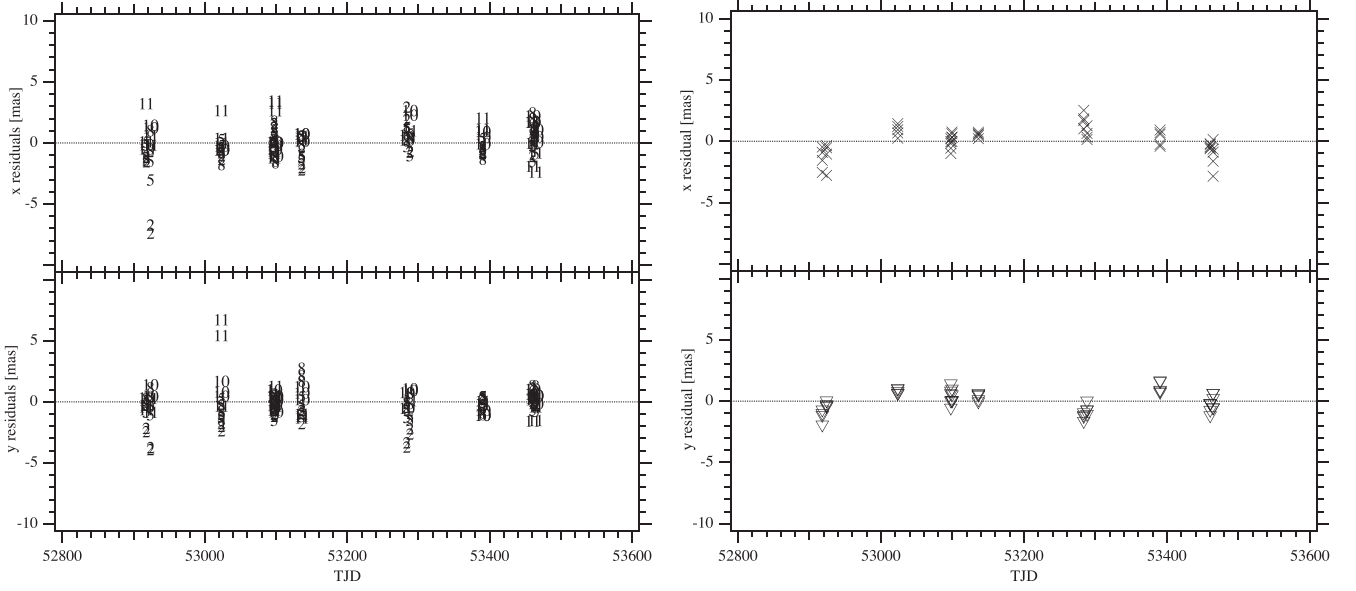
Figure 10. ζ Gem results from Step 3. Right: ζ Gem position residuals plotted against TJD, re-determining coefficients *A–F* in Equations (4)–(7) while solving for η Aql parallax and proper motion. Compared to Figure 8, allowing ζ Gem to assist in determining *A–F* has reduced the ζ Gem rms residuals from (*x*, *y*) = (1.8, 1.6 mas) to (1.5, 1.3 mas), but left the parallax value, $\varpi = 3.11 \pm 0.20$ mas, close to the Gaia EDR3 value. Left: reference star residuals. Compared to Figure 7, allowing the ζ Gem measurements to inform the coefficients *A–F* has increased the reference star residuals rms from (*x*, *y*) = (1.3, 1.2 mas) to (1.5, 1.3 mas).

Table 12
Step 3: Cepheid Parallax, Proper Motion, and Absolute Magnitude

Parameter	Value
η Aql	
ϖ	6.13 ± 0.17 mas
μ_α	7.62 ± 0.17 mas yr^{-1}
μ_δ	-7.39 ± 0.20 mas yr^{-1}
$\boldsymbol{\mu}$	10.62 mas yr^{-1}
P.A.	134°1
LKH corr.	-0.01 mag
Field A_K	0.05 mag
$(m - M)_0$	6.11 mag
M_K	-4.15 ± 0.06 mag
ζ Gem	
ϖ	3.11 ± 0.20 mas
μ_α	-7.58 ± 0.31 mas yr^{-1}
μ_δ	-0.26 ± 0.18 mas yr^{-1}
$\boldsymbol{\mu}$	7.58 mas yr^{-1}
P.A.	268°1
LKH corr.	-0.03 mag
Field A_K	0.02 mag
$(m - M)_0$	7.57 mag
M_K	-5.58 ± 0.14 mag
ζ Gem[a]	
ϖ	2.78 ± 0.18 mas
μ_α	-6.18 ± 0.15 mas yr^{-1}
μ_δ	$+0.20 \pm 0.21$ mas yr^{-1}
$\boldsymbol{\mu}$	6.2 mas yr^{-1}
P.A.	272°
LKH corr.	-0.03 mag
Field A_K	0.02 mag
$(m - M)_0$	7.81 mag
M_K	-5.73 ± 0.14 mag

Note.
[a] Result from Benedict et al. (2007), using parallax priors derived spectro-photometrically and proper motion priors from UCAC2 (Zacharias et al. 2004).

noise seen in Step 2 when compared to the reference star residuals in Step 1, and (ii) that η Aql B causes the η Aql parallax obtained in Step 2 and Step 3 that is significantly larger than EDR3.

With these residual rms excesses, 0.7 to 0.8 mas for η Aql A, now hypothesized to be due to orbital motion, we produce a root sum of squares perturbation, rss = 1.1 mas, which we will use below as a constraint on perturbation period. Comparing ζ Gem residual rms with reference star residual rms, we find rms differences of 0.2–0.4 mas, depending on the axis. The excess ζ Gem residual noise seen in Step 2 when compared to the reference star residuals in Step 1 yields an rss = 0.44 mas. Presuming no ζ Gem companion, the ζ Gem rss provides only weak evidence for the significance of the η Aql rss signature, which is only 2.5× as large.

Also reducing the effectiveness of this approach, neither Cepheid residual time series evidences unexpected and significant peaks in a periodogram. With effectively five or six observations and relatively uniform spacing (mandated by scheduling at maximum parallax factors, with a few in between), Lomb–Scargle periodograms (Figure 14) of the astrometric residuals in Figure 8 yield for ζ Gem only peaks that are either near one year or an alias of one year. The η Aql residuals exhibit only a broad periodogram peak near one-third of a year.

4.3.1. Excess Residual Noise

The astrometry of Step 2 provides no information on the η Aql A–B orbit other than that of the existence of excess astrometric noise, which we now ascribe to a perturbation caused by η Aql B. One might argue that the only valid comparison produced by Step 2 involves differencing the η Aql residual rms (1.8, 1.6 mas) and the ζ Gem values (1.7, 1.4) in Figure 8, for an insignificant rss = 0.22 mas. The astrometric counterargument: we expect the ζ Gem residuals to

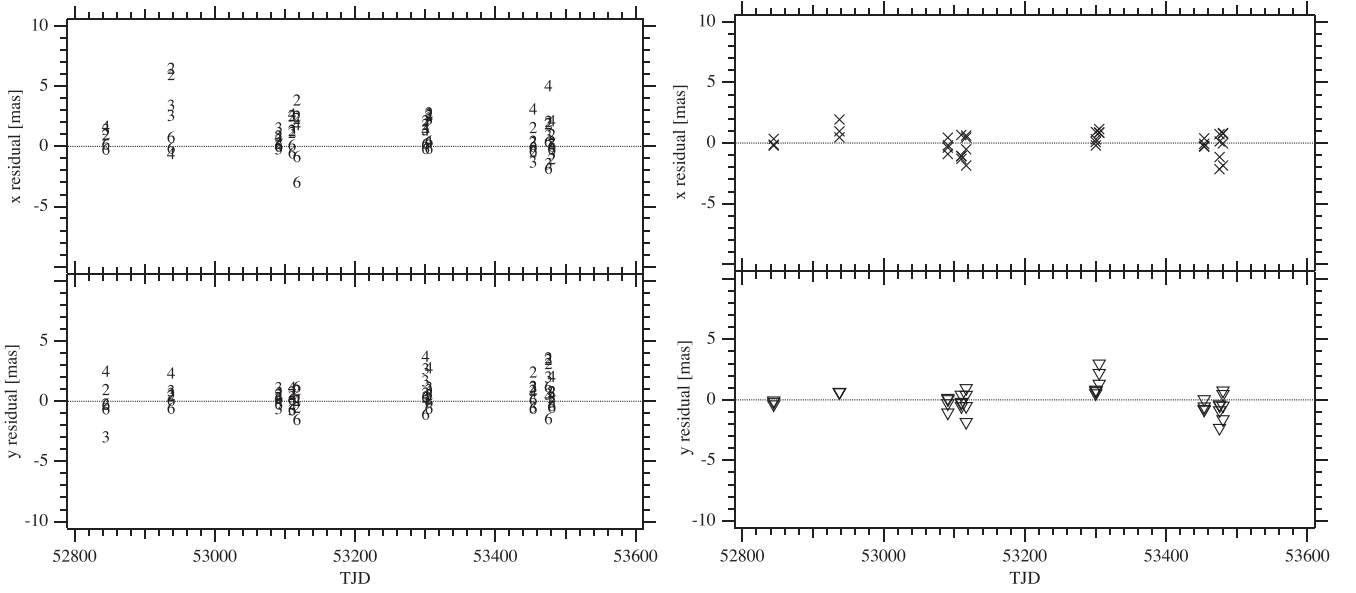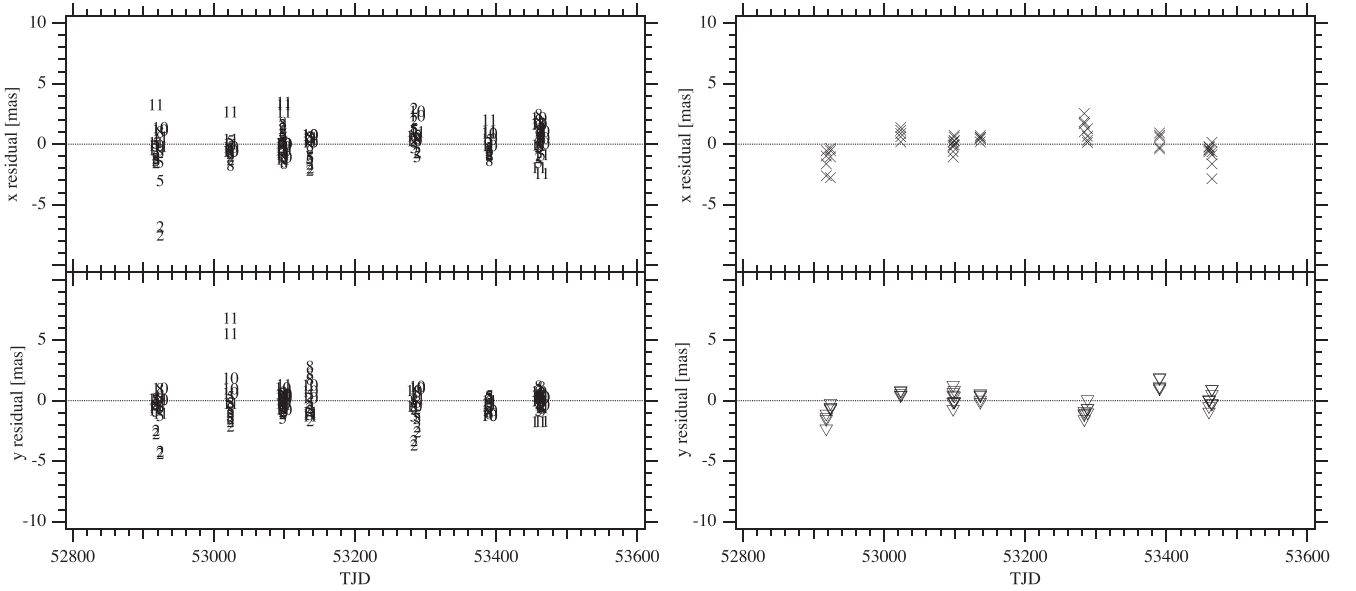**Figure 11.** η Aql results from Step 4. Right: η Aql position residuals plotted against TJD, re-determining the coefficients A–F in Equations (4)–(7) while solving for η Aql parallax and proper motion, including EDR3 priors for all stars. Compared to Figure 8, allowing η Aql to assist in determining A–F has significantly reduced the rms residuals from $(x, y) = (1.8, 1.6$ mas) to $(0.9, 1.0$ mas). Left: reference star residuals. Compared to Figure 7, including the η Aql measurements has significantly increased the reference star residuals rms from $(x, y) = (1.1, 0.8$ mas) to $(1.9, 1.3$ mas).

Figure 12. ζ Gem results from Step 4. Right: ζ Gem position residuals plotted against TJD, re-determining the coefficients A–F in Equations (4)–(7) while solving for ζ Gem parallax and proper motion, including EDR3 priors for all stars. Compared to Figure 8, allowing ζ Gem to assist in determining A–F has reduced the rms residuals from $(x, y) = (1.8, 1.6$ mas) to $(1.1, 0.9$ mas). Left: reference star residuals. Compared to Figure 7, including the ζ Gem priors from EDR3 has increased the reference star residuals rms from $(x, y) = (1.3, 1.2$ mas) to $(1.5, 1.3$ mas).

be large because the ζ Gem reference frame is noisier (Figure 7). Only if the two reference frame noise characteristics were similar (they are not; see Figure 6) would a direct η Aql–ζ Gem comparison yield possible information about η Aql B.

To establish mass limits for η Aql B, we appeal to the literature. The established spectral type, B9.8V, is quite close to A0V, a spectral type for which a recent astrometric mass determination exists (Bond et al. 2017). They find for Sirius, $\mathcal{M}_A = 2.06 \pm 0.02\ \mathcal{M}_\odot$. Including this, we obtain a range of possible B9V–A0V star masses; $\langle \mathcal{M} \rangle = 2.5\ \mathcal{M}_\odot$ from binary star astrometry (Torres et al. 2010), $\langle \mathcal{M} \rangle = 2.9\ \mathcal{M}_\odot$ from

stellar models (Aidelman et al. 2015), hence $2.1 < \mathcal{M}_B < 2.9\ \mathcal{M}_\odot$, not a particularly tight constraint.

To obtain period limits for η Aql B we utilize the mass function, $f(\mathcal{M})$,

$$f(\mathcal{M}) = \frac{\alpha^3}{P^2} = \frac{\mathcal{M}_B^3}{(\mathcal{M}_A + \mathcal{M}_B)^2}. \qquad (8)$$

We next assume a mass for the Cepheid, $\mathcal{M}_A = 5.7\ \mathcal{M}_\odot$ (Evans et al. 2013), our range of possible masses for η Aql B, and an estimated perturbation of 1.1 mas from Section 4.2. We scale α

Table 13
Step 4: Parallax, Proper Motion, and Absolute Magnitude

Parameter	Value
η Aql	
ϖ	3.71 ± 0.07 mas
μ_α	8.89 ± 0.05 mas yr^{-1}
μ_δ	-8.31 ± 0.06 mas yr^{-1}
$\boldsymbol{\mu}$	12.16 mas yr^{-1}
P.A.	$133°1$
LKH corr.	-0.00 mag
Field A_K	0.05 mag
$(m - M)_0$	7.20 mag
M_K	-5.22 ± 0.04 mag
ζ Gem	
ϖ	3.08 ± 0.06 mas
μ_α	-7.73 ± 0.08 mas yr^{-1}
μ_δ	-0.91 ± 0.06 mas yr^{-1}
$\boldsymbol{\mu}$	7.79 mas yr^{-1}
P.A.	$263°3$
LKH corr.	-0.00 mag
Field A_K	0.02 mag
$(m - M)_0$	7.56 mag
M_K	-5.57 ± 0.04 mag

to astronomical units by adopting the Gaia EDR3 parallax, $\varpi = 3.67$ mas. With these assumptions a 1.1 mas perturbation could be caused by this range of possible masses, $2.9 > \mathcal{M}_B > 2.1~\mathcal{M}_\odot$, with this range of possible periods, $0.30 > P_B > 0.15$ yr ($110 > P_B > 55$ days), semimajor axis values in the range $0.89 > a > 0.58$ au, and the range of A–B separation on the sky $3.0 > a > 2.1$ mas. We summarize these results in Table 14. Note that all a values comfortably exceed the interferometrically measured maximum radius of η Aql, $R_{\max} = 0.25$ au (Mérand et al. 2015). Note that the Gaia EDR3 η Aql parallax value yields an absolute K-band magnitude that agrees very well with that predicted by the Benedict et al. (2007) LL (Figure 13). The Gaia Observation Forecast Tool (https://gaia.esac.esa.int/gost/) suggests that the average spacing of η Aql measurements included in EDR3 was ∼22 days. With an estimated period, $P_B \sim 80$ days, is it possible that the 31 observational epochs used to produce the EDR3 parallax value have averaged out any perturbations caused by η Aql B?

Our derived periods are far shorter than those predicted from the common-envelope evolution studies of Neilson et al. (2015), who found it exceedingly unlikely that any Cepheid companion could have $P < 1$ yr. However, η Aql is a triple system. Post-red-giant changes in orbit could be possible via the Kozai–Lidov effect, which can shrink the semimajor axis of an orbit (Naoz 2016).

4.3.2. Anomalous Parallax and η Aql B

The Step 3 modeling yields a parallax, $\varpi = 6.13 \pm 0.17$ mas, still exceeding the Gaia EDR3 value, but with η Aql residuals smaller than seen in Step 2. If the reference frame includes η Aql, the η Aql residuals decrease. This casts doubt on the wisdom of appealing to residual rms for perturbation size (Section 4.3.1). Also, our period range violates the Neilson et al. (2015) limits. The η Aql Step 3 parallax, $\varpi = 6.13 \pm 0.17$ mas, differs from the EDR3 value, $\varpi = 3.67 \pm 0.19$ mas, by $\Delta\varpi = 2.46 \pm 0.25$ mas. Our second hypothesis, breathtakingly ad hoc, supposes that the

η Aql A–B orbital period is close to one year, a period, though unlikely, permitted by the Neilson et al. (2015) results. Hence, that perturbation has an amplitude $\alpha = 2.46$ mas. Our previous loose η Aql B mass constraint was $2.9 > \mathcal{M}_B > 2.1~\mathcal{M}_\odot$. Equation (8), with $P = 1$ yr, $\mathcal{M}_A = 5.7~\mathcal{M}_\odot$, $\alpha = 2.46$ mas, and a scaling parallax, $\varpi = 3.67 \pm 0.19$ mas, yields $\mathcal{M}_B = 1.9 \pm 0.2$ $\mathcal{M}_\odot$. That the EDR3 parallax should have been similarly affected by a period of one year for the AB system argues for the shorter periods discussed in Section 4.3.1.

4.4. Photometry-induced Image Motion

4.4.1. FGS Response to Non-point Sources

FGS position mode works best with point sources. Non-point sources will reduce the amplitude of the interferometric response curve (Nelan 2012, Section 3.5), decreasing the slope of the response curve and thereby degrading the positional precision. η Aql varies in size from 1.65 to 1.85 mas as a function of Cepheid pulsational phase with a maximum near Phase $= 0.4$ (Mérand et al. 2015). ζ Gem varies from 1.6 to 1.75 mas with a maximum near Phase $= 0.25$ (Breitfelder et al. 2016). Inspecting the Step 2 residuals, neither shows an increase in positional scatter at phases of maximum diameter. We conclude that (Cepheid) size does not matter.

4.4.2. A β Constraint?

Heintz (1978) defines a luminosity ratio

$$\beta = L_B / (L_A + L_B) = 1 / (1 + 10^{0.4\Delta m}) \qquad (9)$$

where L is measured luminosity and Δm the magnitude difference between components η Aql A and η Aql B, and a mass fraction, f, calculated from the masses of components A and B,

$$f = \mathcal{M}_B / (\mathcal{M}_B + \mathcal{M}_A). \qquad (10)$$

For this purpose we adopt a distance modulus, $m - M = 7.20$ (Table 13), thus an η Aql absolute magnitude range $-2.9 > M_V > -3.8$, the variation due to Cepheid pulsation. With η Aql B $M_V = 1.17$ (Evans 1991), Cepheid variability produces a variable Δm, hence a variable β, $0.023 > \beta > 0.010$. (The F1-5 V star, η Aql C with $M_V \simeq 3$, contributes little to β.) For the mass fraction we adopt $f = 0.3$ from $\mathcal{M}_A = 5.7~\mathcal{M}_\odot$ and $\mathcal{M}_B = 2.5~\mathcal{M}_\odot$. At any time Component B is $1 - f$ distant from the center of gravity of the system, and $(1 - f) + (f - \beta)$ distant from the center of light (the photocenter). The brighter component A is β distant from the photocenter. Being very small, the changing β has very little leverage to change the small separations between A and B hypothesized in Sections 4.3.1 and 4.3.2, hence the measured position of the brighter component, η Aql A.

Thus far we treated a variation in photocenter position as a nuisance, a source of astrometric noise described through the β parameter. We now turn this around and use β as a probe. The η Aql AB system has a constant photometric source, η Aql B some unknown A–B separation, ρ_{AB}, from a known variable source, η Aql A. The variable $0.023 > \beta > 0.010$ has a vanishingly small effect on smaller separations (Sections 4.3.1 and 4.3.2). For large separations, the η Aql A residuals should correlate with β, a larger β associated with a larger shift from the average photocenter. Demonstrably, β does not strongly

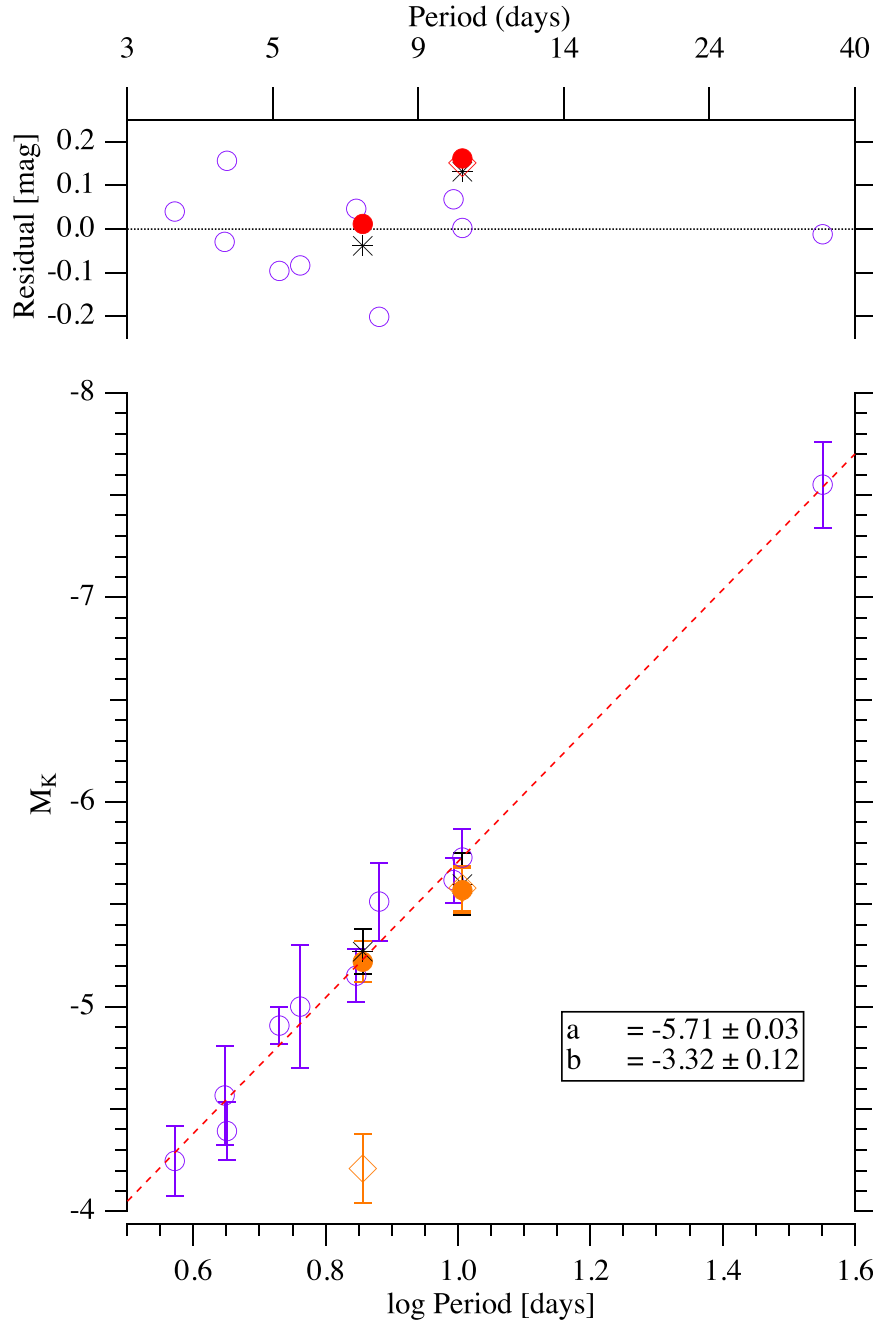**Figure 13.** The K-band LL of Benedict et al. (2007) (○) with the results of Step 3 (◇) in Table 12 and Step 4 (●) in Table 13 for η Aql and ζ Gem now included at log P values of 0.8559 and 1.0065, respectively. M_K values derived from Gaia EDR3 parallaxes are denoted (∗). The slope and intercept of the linear fit are those previously reported. For ζ Gem a model (Step 3) with no EDR3 priors produces a parallax and M_K agreeing with the LL. Exactly the same model with no EDR3 priors applied to η Aql yields a highly discrepant M_K, with a residual ($\Delta M_K = +1.06$) falling outside the range of the residual plot. Including (Step 4) Gaia EDR3 priors for η Aql parallax and proper motion yields agreement with the LL (Table 13).

correlate with astrometric residual as shown in Figure 15. This lack of correlation supports small separations.

We now attribute the excess residual (comparing η Aql residuals with the reference star residuals) found in Step 2 only to photocenter variations. We have identified a residual difference 0.7 mas in R.A. and 0.8 mas in decl. between the position measurements of η Aql A and those of the reference stars. We now hypothesize that this difference is due to β alone, working on an unknown ρ_{AB}. $\rho_{AB} = 200$ mas would cause

photocenter motion due only to Cepheid pulsation, varying between 2.4 and 4.4 mas, $\Delta \rho_{AB} = \pm 1.0$ mas, centered on the average η Aql $\beta = 0.015$. This variation is of the same order of magnitude as the excess residuals from Section 4.2. A separation, $\rho_{AB} = 200$ mas, and a position angle, P.A. = 45°, produce the lines in Figure 15, intersecting the brightest ($\beta = 0.012$) and faintest ($\beta = 0.022$) phases. The residual pattern in Figure 15 is consistent with a separation $\rho_{AB} = 200$ mas and position angle P.A. = 45°. Assuming
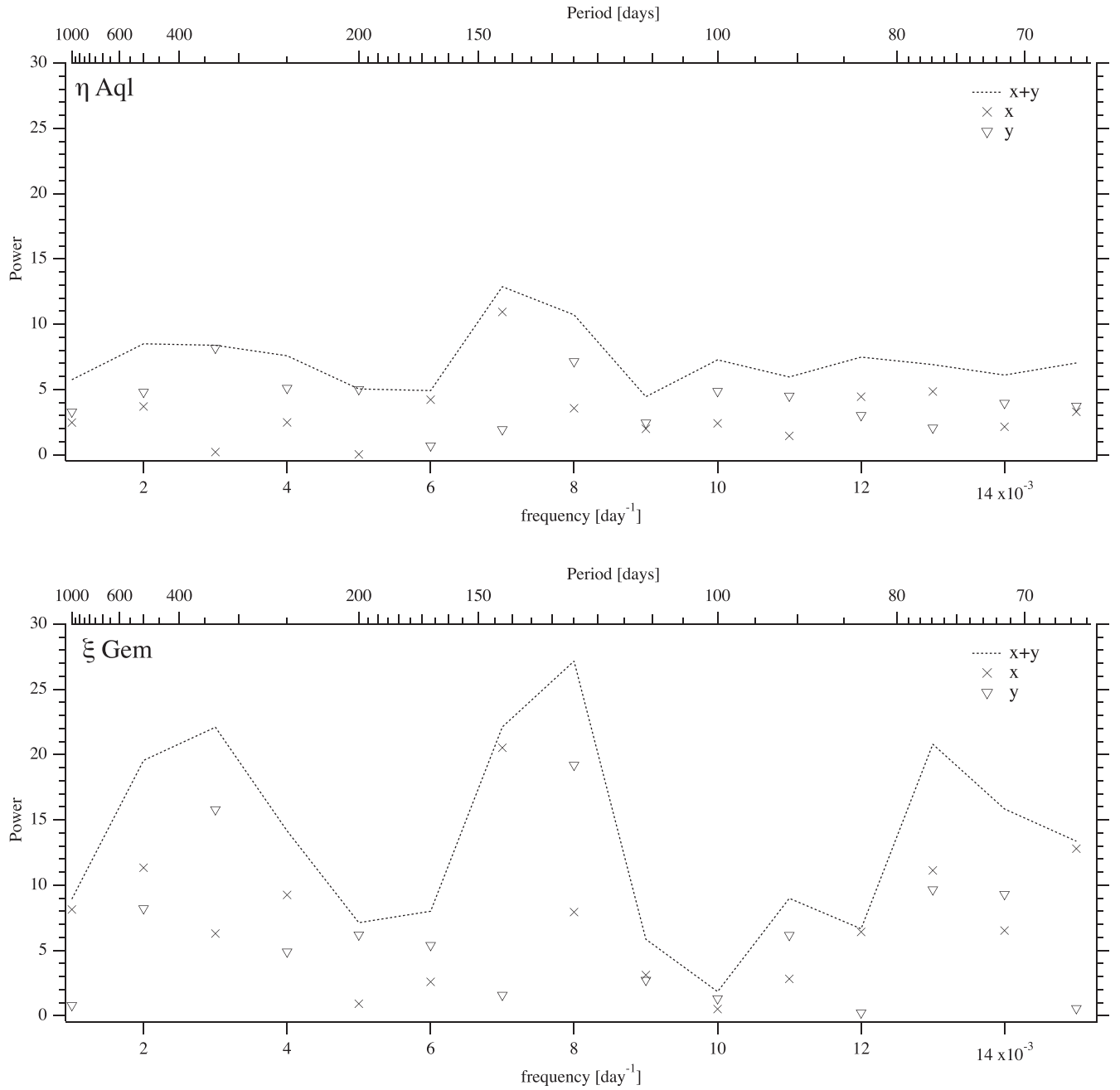
Figure 14. Lomb–Scargle periodogram of the Step 2 residuals in Figure 8. ζ Gem exhibits significant power (false alarm probability (FAP) ≪ 0.001%) near one year or aliases of that period. η Aql residuals exhibit a broad peak near 133 days with FAP ∼ 0.1%.

Table 14
η Aql A–B Period Range from η Aql B Mass Range

$\mathcal{M}_A$	$\mathcal{M}_B$	P (yr)	P (days)	a (au)	α (au)	α (mas)	a (arcsec)
5.7	2.1	0.27	97	0.82	0.3	1.1	0.0030
5.7	2.2	0.25	91	0.79	0.3	1.1	0.0029
5.7	2.3	0.23	84	0.75	0.3	1.1	0.0028
5.7	2.7	0.18	66	0.65	0.3	1.1	0.0024
5.7	2.9	0.15	55	0.58	0.3	1.1	0.0021
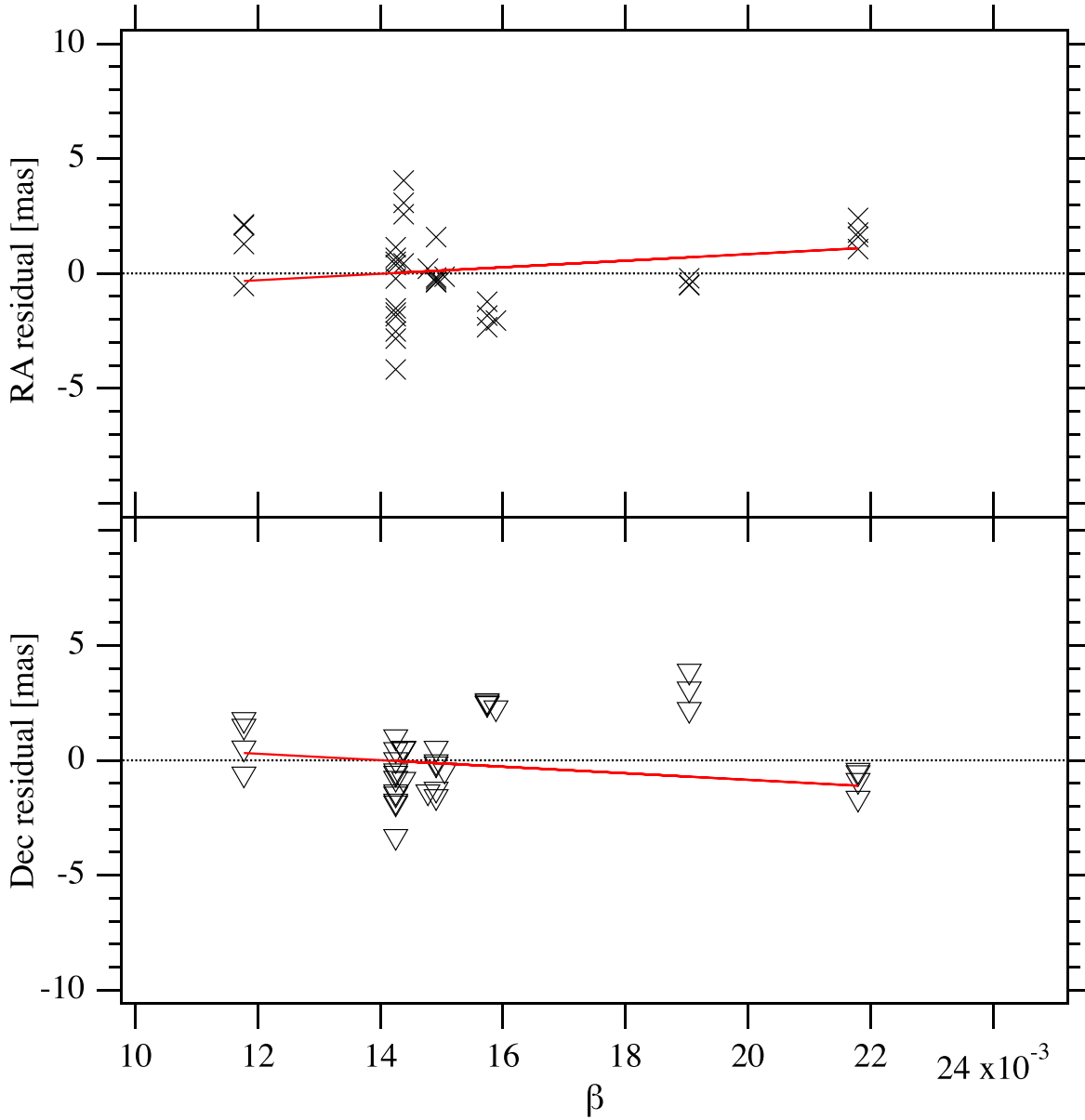
Figure 15. The η Aql A position residuals of Step 2 vs. the β parameter of Section 4.4.2, showing no strong correlation The lines linking the smallest and largest measured β values (while passing near the average $\beta = 0.015$) indicate what variation might be caused by an η Aql AB system with separation $\rho_{AB} = 200$ mas at position angle P.A. = 45°.

$\mathcal{M}_A = 5.7 \, \mathcal{M}_\odot$ and $\mathcal{M}_B = 2.2 \, \mathcal{M}_\odot$ yields $P_{AB} = 152$ yr, and undetectable RV variations (± 1 km s^{-1}) for inclinations less than $\sim 20°$. These residual $= f(\beta)$ distributions lack the signal-to-noise ratio to serve as compelling evidence, but do serve to illustrate a possible technique.

5. Summary

1. More precise data from the HET HRS, the Hermes spectrograph on the Mercator Telescope, the Coralie spectrograph on the Euler Telescope, the HJS Telescope, and previously obtained lower-precision measurements, yield a Cepheid pulsational RV curve, adequately described by a Fourier series with 12 coefficients.

2. The lack of any detectable period in the RV residuals obtained by removing the Cepheid RV signature suggests either a nearly face-on orbit or a very long period for the η Aql A–B system.

3. Astrometry (Step 1) of the reference stars associated with η Aql and ζ Gem demonstrates precision of 0.6 mas and 1 mas per observation respectively.

4. An astrometric reanalysis (Steps 2 through 4) of the ζ Gem field yields a parallax agreeing with both Gaia EDR3 and Benedict et al. (2007), establishing the robustness of our astrometric modeling.

5. η Aql HST/FGS astrometry (Steps 2 and 3) carried out with no prior knowledge of parallax or proper motion resulted in a parallax yielding an absolute K-band magnitude approximately one magnitude fainter than that predicted by the Benedict et al. (2007) LL, and with positional residual rms larger than that obtained for the reference stars.

6. Including (Step 4) parallax and proper motion priors from Gaia EDR3 for reference stars and η Aql resulted in better agreement with EDR3 (with errors smaller than EDR3)

and smaller positional residuals for η Aql, but at the expense of significantly larger residuals in the reference stars.

7. Neither the Gaia EDR3 RUWE nor the Brandt (2021) χ^2 values are consistent with astrometric companions for either η Aql or ζ Gem.

8. Comparing the η Aql residuals of Step 2 to the reference star residuals, we determine that η Aql exhibits an rms excess of $\sim$1.1 mas. Assuming the excess comes from orbital motion, assuming a mass $\mathcal{M}_A = 5.7\ \mathcal{M}_\odot$ for η Aql A, and assuming a range of possible masses $2.9 > \mathcal{M}_B > 2.1\ \mathcal{M}_\odot$ for η Aql B provides a possible period range of $0.15 < P_B < 0.30$ yr ($110 > P_B > 55$ days). The Gaia average measurement spacing of $\sim$22 days may have averaged out this perturbation. However, to find a Cepheid companion with this short a period is highly unlikely, and might require the effects of Kozai–Lidov on the orbit.

9. Hypothesizing that the parallax mismatch between the Step 3 FGS result and the Gaia EDR3 result represents a perturbation amplitude from an η Aql A–B orbit with $P = 1$ yr suggests $\mathcal{M}_B = 1.9 \pm 0.2\ \mathcal{M}_\odot$. That the EDR3 parallax result is not similarly affected argues against this hypothesis.

10. Ascribing photocenter motion only to the variation of the Cepheid, η Aql A, in the presence of the constant brightness companion, η Aql B, and working only with the brightest and faintest Cepheid phases yields a possible separation $\rho_{AB} \sim 200$ mas at a position angle P.A. $\sim 45°$, a separation consistent with a long period ($\sim$150 yr) and the observed extremely small RV variation. The residual $= f(\beta)$ relations are too noisy to constitute a firm measurement of P.A. and ρ of an actual binary system.

11. None of these efforts to further characterize the companion η Aql B obtained through hypothesis provide any actual η Aql B orbit information, only results based on conjectures engendered by peculiarities in the astrometric results, which could be previously unidentified systematic errors.

ORCID iDs

G. Fritz Benedict https://orcid.org/0000-0003-2852-3279
Thomas G. Barnes, III https://orcid.org/0000-0002-3557-1239
Nancy R. Evans https://orcid.org/0000-0002-4374-075X
William D. Cochran https://orcid.org/0000-0001-9662-3496
Richard I. Anderson https://orcid.org/0000-0001-8089-4419
Thomas E. Harrison https://orcid.org/0000-0003-4917-387X

References

Aidelman, Y., Cidale, L. S., Zorec, J., et al. 2015, A&A, 577, A45
Anderson, R. I., Casertano, S., Riess, A. G., et al. 2016, ApJS, 226, 18
Barnes, T. G., III, Fernley, J. A., Frueh, M. L., et al. 1997, PASP, 109, 645
Barnes, T. G., III, Jeffery, E. J., Montemayor, T. J., et al. 2005, ApJS, 156, 227
Belokurov, V., Penoyre, Z., Oh, S., et al. 2020, MNRAS, 496, 1922
Benedict, G. F., McArthur, B., Nelan, E. P., et al. 1998, Proc. SPIE, 3350, 229
Benedict, G. F., McArthur, B. E., Feast, M. W., et al. 2007, AJ, 133, 1810
Benedict, G. F., McArthur, B. E., Feast, M. W., et al. 2011, AJ, 142, 187
Benedict, G. F., McArthur, B. E., Nelan, E. P., et al. 2017, PASP, 129, 012001
Berdnikov, L. N., Ignatova, V. V., Caldwell, J. A. R., et al. 2000, NewA, 4, 625
Berdnikov, L. N. 2008, yCat, II/285
Bersier, D. 2002, ApJS, 140, 465
Bond, H. E., Schaefer, G. H., Gilliland, R. L., et al. 2017, ApJ, 840, 70
Borgniet, S., Kervella, P., Nardetto, N., et al. 2019, A&A, 631, A37
Brandt, T. D. 2021, ApJS, 254, 42
Breitfelder, J., Mérand, A., Kervella, P., et al. 2016, A&A, 587, A117
Cochran, W. D., Endl, M., McArthur, B., et al. 2004, ApJL, 611, L133
Eaton, J. A. 2020, JAVSO, 48, 91
Eaton, J. A., & Williamson, M. H. 2007, PASP, 119, 886
Engle, S. 2015, PhD thesis, James Cook University
Evans, N. E., Bond, H. E., Schaefer, G. H., et al. 2013, AJ, 146, 93
Evans, N. R. 1991, ApJ, 372, 597
Evans, N. R. 2000, AJ, 119, 3050
Evans, N. R., Berdnikov, L., Lauer, J., et al. 2015, AJ, 150, 13
Gaia Collaboration, Brown, A. G. A., Vallenari, A., et al. 2021, A&A, 649, A1
Gallenne, A., Kervella, P., Mérand, A., et al. 2014, A&A, 567, A60
Heintz, W. D. 1978, Double Stars (Dordrecht: Reidel)
Jefferys, W. H., Fitzpatrick, M. J., & McArthur, B. E. 1988, CeMec, 41, 39
Kiss, L. L., & Vinkó, J. 2000, MNRAS, 314, 420
Lindegren, L., Klioner, S. A., Hernández, J., et al. 2021, A&A, 649, A2
Marcy, G. W., & Butler, R. P. 1992, PASP, 104, 270
Mariska, J. T., Doschek, G. A., & Feldman, U. 1980, ApJL, 238, L87

McArthur, B., Benedict, G. F., Jefferys, W. H., et al. 2002, in The 2002 HST Calibration Workshop: Hubble after the Installation of the ACS and the NICMOS Cooling System, ed. S. Arribas, A. Koekemoer, & B. Whitmore (Baltimore, MD: Space Telescope Science Institute), 373
Mérand, A., Kervella, P., Breitfelder, J., et al. 2015, A&A, 584, A80
Moffett, T. J., & Barnes, T. G. I. 1980, ApJS, 44, 427
Naoz, S. 2016, ARA&A, 54, 441
Neilson, H. R., Schneider, F. R. N., Izzard, R. G., et al. 2015, A&A, 574, A2
Nelan, E. E. 2012, Fine Guidance Sensor Instrument Handbook for Cycle 21 v.20.0 (Baltimore, MD: STScI)

Skrutskie, M. F., Cutri, R. M., Stiening, R., et al. 2006, AJ, 131, 1163
Standish, E. M., Jr. 1990, A&A, 233, 252
Stassun, K. G., & Torres, G. 2021, ApJL, 907, L33
Storm, J., Carney, B. W., Gieren, W. P., et al. 2004, yCat, J/A+A/415/531
Torres, G., Andersen, J., & Giménez, A. 2010, A&ARv, 18, 67
Tull, R. G. 1998, Proc. SPIE, 3355, 387
Tull, R. G., MacQueen, P. J., Sneden, C., et al. 1995, PASP, 107, 251
Welch, D. L., Wieland, F., McAlary, C. W., et al. 1984, ApJS, 54, 547
Wright, J. T., & Eastman, J. D. 2014, PASP, 126, 838
Zacharias, N., Urban, S. E., Zacharias, M. I., et al. 2004, AJ, 127, 3043